

1 Kinetic and equilibrium reactions on natural and laboratory generation
2 of thermogenic gases from Type II marine shale

3

4

Xiaoqiang Li* and Juske Horita

5

Department of Geosciences, Texas Tech University, Lubbock, TX 79409, USA

6

(*Corresponding author: xiaoqiang.li@ttu.edu)

7

8 **Abstract**

9 The phenomenon that laboratory pyrolysis experiments produce much wetter gases than those in
10 natural reservoirs is a long-recognized and debated problem in the investigation of natural gases
11 in sedimentary basins. In this study, we explore the discrepancy by pyrolyzing a type II kerogen
12 from the Woodford Shale in Oklahoma, compared with the previous results on the produced
13 natural gases from the Arkoma Basin generated from the same source rock (Liu et al., 2019) with
14 the discussion of gas and isotopic compositions at bulk and position-specific (PS) levels. An
15 improved GC-pyrolysis-GC IRMS method is applied for the determination of PS $\delta^{13}\text{C}$ of propane
16 produced in the pyrolysis of the Woodford Shale at Easy $\%R_o$ from 0.76 to 3.27. Kinetic and
17 thermodynamic considerations of the chemical and isotopic compositions of the natural and
18 laboratory pyrolysis gases suggest that the generation of light hydrocarbons involves uni-
19 directional cracking reactions, exchange reactions with water, and likely reversible reactions
20 among light hydrocarbons and other H-containing volatiles. After the gas generation in the
21 unconventional Woodford Shale reservoirs, the $\text{C}_1\text{-C}_4$ gases might have approached close to

22 chemical equilibrium of C₁-C₃ and isotope equilibrium of C₂-C₁ and C₃-C₁ pairs at their peak
23 temperatures. The capping H for the generation of C₁-C₄ in the Woodford Shale gases appears to
24 have experienced at least partial exchange with the water, while that in the pyrolysis gases is only
25 originated from organic-bound compounds with large kinetic isotope effects (KIE). Our findings
26 indicate that elevated compound-specific and PS δ¹³C values of propane in the wet-gas cracking
27 stage are significantly influenced by the breakdown of the thermally stable compounds (e.g.,
28 remaining kerogen, residues). A first synthesis of PS δ¹³C and δ²H isotopic compositions of
29 propane from this study and the literature data suggests relatively similar isotopic structures of
30 propane precursors in kerogens. This study demonstrates that PS isotope analysis of propane can
31 contribute to identifying various geological (e.g., maturation, wet-gas cracking, H exchange,
32 diffusion) and biodegradation processes.

33 **Key words:** natural gas, pyrolysis gas, Woodford Shale, position-specific isotope, H exchange

34

35 1 Introduction

36 Chemical and isotopic compositions of hydrocarbon gases in sedimentary basins have been
37 traditionally applied to trace natural gas history, including the source and secondary alteration (e.g.,
38 Bernard et al., 1976; Schoell, 1988; Whiticar, 1999). In order to understand gas generation in
39 natural reservoirs, artificial simulation of sedimentary organic matter maturation has been
40 extensively applied. However, the laboratory experiments tend to produce wet pyrolysis gases
41 (CH₄ mole contents: 10 - 60%), which are different from much drier gases (70 - 99%) in the
42 conventional and unconventional reservoirs (e.g., Horsfield et al., 1992; Behar et al., 1997). Causes
43 for these well-documented differences between laboratory pyrolysis and natural gases have been

44 extensively debated. In summary, the discrepancy of the gas dryness between natural reservoirs
45 and pyrolysis experiments has been explained by several factors: secondary alteration (migration,
46 oxidative degradation/biodegradation, mixing of gases from different origins or maturities) (e.g.,
47 Price and Schoell, 1995) and catalytic equilibrium processes (e.g., Mango, 1992; Mango et al.,
48 2009). The catalytic theory is challenged due to the lack of compelling evidence (e.g., Snowdon,
49 2001; Michels et al., 2002; Lewan et al., 2008). In gas migration from source rocks (in-situ gas) to
50 reservoirs, the gas compositions could be altered by several processes: preferential diffusion of
51 lighter hydrocarbons, bacteria degradation and so on. Although gases in conventional reservoirs
52 are unlikely to represent gases generated in-situ in source rocks, unconventional gases in shales
53 serving as both source rock and reservoir are also very dry (CH_4 content: > 95%) (e.g., Rodriguez
54 and Philp, 2010; Zumberge et al., 2012).

55 Recent studies of position-specific (PS) isotope analysis of the volatile hydrocarbons provide new
56 and important constraints on the origins and generation mechanisms of natural gases (Gao et al.,
57 2016; Gilbert et al., 2016; Eiler et al., 2017; Piasecki et al., 2018; Liu et al., 2019; Julien et al.,
58 2020). It has been shown that PS isotope analysis of propane could have significant advantage of
59 discriminating the abiotic and biotic gases (Suda et al., 2017), identifying microbial activities in
60 thermogenic gas (Gilbert et al., 2019; Gilbert, 2021), and testing the intramolecular isotope
61 equilibrium (Liu et al., 2019; Xie et al., 2020) in natural reservoirs. Several methods have been
62 developed to measure the PS carbon and hydrogen isotopes of gaseous hydrocarbons, including
63 high resolution isotope ratio mass spectrometer (HR-IRMS) (Piasecki et al., 2016; Xie et al., 2018),
64 GC-pyrolysis-GC IRMS (Gilbert et al., 2016; Li et al., 2018), chemical degradation method
65 followed by GC IRMS (Gao et al., 2016), and quantitative nuclear magnetic resonance (qNMR)
66 spectrometry (Liu et al., 2018). The GC-pyrolysis-GC IRMS techniques can handle small sample

67 size (~0.1 μmol propane), but cannot demonstrate the accuracy, due to the isotope fractionation in
68 C_3H_8 pyrolysis processes. The qNMR technique, which requires relatively large amounts (~6
69 mmol) of propane to determine position-specific C and H isotopes, is the only method with high
70 accuracy and precision.

71 Here, we firstly present an improved GC-Py-GC IRMS method combined with the qNMR
72 technique to accurately and precisely measure PS C isotope compositions of small-sized propane.
73 Then, we conduct a series of systematic experiments of hydrous and anhydrous pyrolysis of a type
74 II kerogen from the Woodford Shale in Oklahoma, United States, and integrate the previous results
75 on the natural gases from the same source rock (Liu et al., 2019), including the gas compositions,
76 carbon and hydrogen bulk isotopes, and PS $\delta^{13}\text{C}$ of propane. The goal of this synthesis study of
77 the natural and pyrolysis gases from the Woodford Shale includes: (a) demonstrating differences
78 in the geochemistry of gas generation under natural and laboratory conditions from the same
79 source rock, (b) modeling and understanding the importance of kinetic/equilibrium isotopic effects
80 and exchange reactions on gaseous and isotopic compositions, and (c) laying a framework for
81 interpreting the PS isotope compositions of propane in nature. To our knowledge, this is the first
82 study to decipher in detail the discrepancy between the pyrolysis and natural gases from the same
83 source rock to better understand the history of gases in natural reservoirs.

84 2 Samples and Experiments

85 2.1 Samples

86 The Upper Devonian-Lower Mississippian Woodford Shale was collected from a road outcrop
87 along Interstate 35 in the south flank of the Arbuckle Anticline, Ardmore Basin, Oklahoma for
88 hydrous and anhydrous pyrolysis experiments, which was also used in the previous studies (e.g.,

89 Lewan, 1997; Shuai et al., 2018; Shao et al., 2020). This sample has a TOC (total organic carbon)
90 value of 15.9 wt%, TN (total nitrogen) content of 0.5 wt%, organic sulfur content of 0.7 wt%
91 (Craddock et al., 2018), HI (hydrogen index) value of 535 mg HC (hydrocarbon) /g TOC, and a
92 T_{\max} (temperature of maximum hydrocarbon generation rate) of 419 °C. The kerogen of the
93 Woodford Shale is type II with the thermal maturity ($\%R_o$) of 0.38 based on the T_{\max} values (Jarvie
94 et al., 2001). This immature sample is relatively quartz-rich (51.3%), containing 21.1% mica, 5.8%
95 K-feldspar, 3.2% pyrite, and 0.8% kaolinite, but no carbonate. The Woodford kerogen has a $\delta^{13}\text{C}$
96 value of -29‰ and $\delta^{15}\text{N}$ of -4.6‰.

97 2.2 Pyrolysis experiments

98 Hydrous pyrolysis experiments were conducted on the Woodford Shale, using a 300 ml bolted-
99 closure Hastelloy reactor vessel at temperatures of 310, 340, and 360 °C for 72h, and 370 °C for
100 16 and 50 days. The experimental procedures were similar to those used by Lewan (1993). 30 -
101 110 g of crushed and sieved rock materials (particle fraction: 0.5 - 2 cm diameter) and 80 - 95 g of
102 deionized (DI) water with a $\delta^2\text{H}$ (VSMOW) value of $-36 \pm 0.2\text{‰}$ were loaded into a quartz liner
103 placed in the reactor, which was connected to a 2-port valve via 1/16 inch OD stainless steel tubing.
104 After checking for leaks by adding ~ 80 psi of air to the vessel and monitoring pressure, the reactor
105 was evacuated to 0.3 psi and placed in a convection oven. A K-type thermocouple, which was
106 closely positioned to the location of the samples outside of the reactor and wrapped by Al foil, was
107 used to monitor the temperature of the reactor within ± 0.5 °C. The temperatures and durations of
108 the hydrous pyrolysis experiments were chosen to simulate gas generation from an early oil
109 window to a late stage of oil cracking. Anhydrous pyrolysis of the Woodford Shale was performed
110 in the same Hastelloy reactor at 310, 340, 360, 400, 415, 430, 450, 470, and 480 °C for 72h. The
111 experimental procedures were similar to those for the hydrous pyrolysis without added water. After

112 loading the samples into the liner, quartz wool was added to prevent the powder from blocking the
113 1/16 inch OD tubes when the reactor was evacuated to 0.1 torr. The temperature conditions
114 employed in this investigation were chosen to simulate the full range of petroleum and gas
115 generation from early oil generation to late wet-gas cracking. In these series of pyrolysis
116 experiments, the temperature-time conditions were converted to Easy %R_o values (Table 1) based
117 on the procedures of Sweeny and Burnham (1990).

118 After cooling down the Hastelloy reactor to room temperature, the gaseous products in the
119 headspace were expanded into a pre-evacuated and calibrated volume connected to a pressure
120 gauge. The total amounts of the gas were calculated based on the temperature and pressure
121 according to the ideal gas law. The gases were extracted by a 10-ml gas-tight syringe through a
122 septum and stored in 10 ml pre-evacuated serum vials for the analysis of chemical and bulk isotope
123 compositions, and position-specific ¹³C isotope of propane.

124 3 Analytical Methods

125 3.1 Chemical and bulk isotope compositions of the gaseous products

126 The analysis of the gaseous components from the pyrolysis of the Woodford Shale as well as their
127 isotopic compositions was carried out, using gas chromatography-combustion/pyrolysis-isotope
128 ratio mass spectrometry (GC-C/Py-IRMS). The gases stored in the serum bottles were injected
129 with a gas-tight syringe and transferred by high-purity helium into a GC column CP7551 (HP-
130 PLOT-Q, 27.5 m long and 0.32 mm ID including a 2.5 m particle trap, 10 μm film thickness),
131 which was connected through a GC Isolink unit to a Finnigan Delta V Plus mass spectrometer.
132 The injector temperature was set at 100 °C with a split ratio of 8. The GC oven temperature was

133 initially kept at 30 °C for 4 min, increased to 100 °C at a heating rate of 6 °C/min, followed by an
134 increase to 220 °C at a heating rate of 20 °C/min, and then kept constant for 2 min.

135 For bulk carbon isotope analysis, about 10 µl of the gas sample was injected and the combustion
136 furnace temperature was set at 1030 °C with a helium flow rate of 1.2 ml/min. For hydrogen
137 isotopic compositions, at least 20 µl of gas was injected, with the temperature of the high-
138 temperature conversion (HTC) reactor set at 1420 °C and a helium flow rate of 1 ml/min. The
139 chemical compositions of the gaseous products (hydrocarbon gases, CO₂, H₂, H₂S) in the pyrolysis
140 experiments were calibrated by injecting varying volumes of a standard hydrocarbon gas mixture
141 (Scotty Calibration Gases), pure H₂ and CO₂, and a gas mixture of H₂S (1% mole concentration)
142 balanced with N₂. In the determination of gas compositions, the errors are mainly sourced from
143 the calibration curves of C₁-C₅, H₂, H₂S and CO₂, which potentially produce the errors of < ± 5%.
144 The bulk carbon and hydrogen isotopic compositions were calibrated against the VPDB and
145 VSMOW scales, respectively, using the natural gas standards obtained from the U.S. Geological
146 Survey (Ellis and Dias, 2022). The precisions of δ¹³C and δ²H are within ± 0.5‰ and ± 5‰,
147 respectively (1 σ).

148 3.2 Position-specific C isotopes of propane

149 For the determination of intramolecular δ¹³C values of propane in the pyrolysis gases, an improved
150 GC-pyrolysis (Py)-GC IRMS method was developed. The working procedures have already been
151 described by Gilbert et al. (2016). Approximately 60 µl gas samples with C₃H₈ contents of ~ 5%
152 were injected via a gas-tight syringe with an injector temperature of 100 °C and a split ratio of 4.
153 In the first GC column (HP-PLOT-Q, 27.5 m × 0.32 mm i.d. including 2.5 m particle trap, 10 µm
154 film thickness) propane was separated from other compounds. The gases were transferred by high
155 purity helium at 2.5 ml/min into a high-temperature pyrolysis furnace connected with the second

156 column (CP-PoraPLOT-Q, 27.5 m long and 0.32 mm ID, 10 μm film thickness) to separate the
157 CH_4 , C_2H_4 and C_2H_6 fragments from propane cracking. The temperature program for the first GC
158 column was initially 50 $^\circ\text{C}$ for 15 min, then increased to 100 $^\circ\text{C}$ at 10 $^\circ\text{C}/\text{min}$ and held for 10 min,
159 and finally heated at 20 $^\circ\text{C}/\text{min}$ to 150 $^\circ\text{C}$ where it was kept for 15 min. The second column was
160 placed in an oven at room temperature during the measurements and heated to 180 $^\circ\text{C}$ after each
161 analysis in order to elute the other longer-chain HCs retained on the column. The temperature in
162 the pyrolysis furnace was set at 800-820 $^\circ\text{C}$, where $\delta^{13}\text{C}$ values of CH_4 , C_2H_4 and C_2H_6 from
163 propane cracking were found to be stable and reproducible. The pyrolysis temperatures in Gilbert
164 et al. (2016) and Li et al. (2018) were 850 $^\circ\text{C}$ and 800 - 840 $^\circ\text{C}$, respectively, which are different
165 from that in this study, due probably to the different arrangement of pyrolysis tube and furnace. In
166 this study at 800-820 $^\circ\text{C}$ we verified that the secondary reactions (e.g., $\text{C}_2\text{H}_6 \rightarrow \text{C}_2\text{H}_4 + \text{H}_2$) were
167 insignificant, by comparing our experimental results with the previous study (Gilbert et al., 2016),
168 including the chemical and isotopic compositions of gaseous products from propane cracking. In
169 the measurements, the smallest peak (C_2H_6) from the propane cracking was large enough (> 600
170 mV) for the determination of the isotopes. The precisions of $\delta^{13}\text{C}$ values at the terminal and central
171 sites of propane are within $\pm 0.3\text{‰}$ (1σ).

172 C isotope fractionation occurs during the propane pyrolysis to the fragments (CH_4 , C_2H_4 and C_2H_6)
173 in the GC-Py-GC IRMS method (Gilbert et al., 2019). To obtain accurate position-specific $\delta^{13}\text{C}$
174 values using the GC-Py-GC IRMS method, instrumental carbon isotope fractionation factors at
175 the terminal and central sites should be determined during the C_3H_8 cracking. Based on the
176 position-specific isotopes of propane from a set of natural gas samples and pure propane, which
177 were previously determined with the qNMR technique (Liu et al., 2019), the isotope fractionation
178 factors for the terminal and the central site in the GC-Py-GC IRMS method were determined and

179 applied for the corrections (Fig. S1). The isotope fractionation factors at the terminal and central
180 sites of propane are $3.5 \pm 0.5\text{‰}$ and $4.8 \pm 1.1\text{‰}$, respectively (1σ). Based on the errors in
181 techniques of qNMR and GC-Py-GC IRMS, the analytical errors of the corrected $\delta^{13}\text{C}$ values at
182 the terminal and central sites are $\sim \pm 0.7$ and $\pm 1.3\text{‰}$, respectively.

183 4 Results

184 The marine Woodford Shale sampled from the I-35 outcrop, Oklahoma, was also pyrolyzed in the
185 previous studies (e.g., Lewan, 1997; Shuai et al., 2018; Shao et al., 2020). Lewan (1997)
186 investigated the role of water in hydrocarbon generation at 300 to 350 °C in the maturity range of
187 0.7 to 1.1 (Easy %R_o) with the quantification of hydrocarbon gases, CO₂, H₂S and H₂, but with no
188 isotope values reported. Shuai et al. (2018) explored the clumped isotopic signatures of CH₄
189 generated in the hydrous pyrolysis experiments at the temperatures of 330 to 415 °C (Easy %R_o:
190 0.9 - 2) without gas yields and isotopic values of C₂₊ gas species. Shao et al. (2020) only reported
191 the total yields of hydrocarbon gases and oil products in the anhydrous conditions at the
192 temperature range from 300 to 425 °C with Easy %R_o of 0.7 to 2.2. In this study, our experimental
193 results were also compared with the isotopic evolution of hydrocarbon gases with thermal
194 maturities in the pyrolysis of other source rocks, for example marine New Albany Shale (Gao et
195 al., 2014) and Cretaceous coal (Ni et al., 2018).

196 4.1 Gas yields

197 The molar yields (mmol/g TOC) of hydrocarbon gases (C₁-C₅) and non-hydrocarbon gases (CO₂,
198 H₂S, H₂) in the hydrous and anhydrous pyrolysis of the Woodford Shale in the temperature range
199 of 310 to 480 °C changed as a function of thermal maturity (Table 1 and Fig. 1). In the hydrous
200 pyrolysis experiments, the yields of CH₄, C₂H₆ and C₃H₈ increased from 0.29 to 3.58, 0.13 to 1.44,

201 and 0.08 to 0.9 mmol/g TOC, respectively, in the Easy %R_o ranging from 0.76 to 1.95. For the
202 anhydrous pyrolysis experiments in the temperature of 310 to 480 °C (Easy %R_o: 0.76 - 3.27), the
203 yields increased from 0.26 to 9.99 and 0.13 to 2.07 mmol/g TOC for CH₄ and C₂H₆, respectively.
204 The yields of C₃H₈, C₄H₁₀ and C₅H₁₂ firstly increased with thermal maturity, then decreased due
205 to the cracking of these compounds. For the unsaturated HC gases, C₂H₄ was under the detection
206 limit and C₃H₆ was produced in the insignificant amounts (< 0.03 mmol/g TOC) in the both
207 hydrous and anhydrous experiments. Based on the evolution of the molar yields of HC gases in
208 the pyrolysis of the Woodford Shale (Fig. 1), the generation of HC gases were divided into 3 stages:
209 kerogen cracking (Easy %R_o: ~ 1.2), oil cracking (Easy %R_o: 1.2 - 2), and wet-gas cracking
210 (Easy %R_o: > 2), which are consistent with the stages based on produced oil yields (Shao et al.,
211 2020).

212 The total hydrocarbon gas (C₁-C₅) yields varied from 0.6 to 6.6 and 0.6 to 12.2 mmol/g TOC in
213 the hydrous and anhydrous pyrolysis experiments, respectively (Fig. 2), matching the kinetic
214 calculations based on gas generation from the immature marine Kimmeridge Clay kerogen (Pepper
215 and Corvit, 1995) and oil cracking (Pepper and Dodd, 1995). Generally, the HC gas yields in the
216 anhydrous conditions were higher than those from the hydrous experiments, which is in line with
217 the experimental results from Lewan (1997). The molar ratios of C₁/(C₁-C₅) (gas dryness) in the
218 hydrous pyrolysis experiments varied between 0.50 and 0.55 in the kerogen and oil cracking stages
219 (Easy %R_o: 0.76 - 1.95) (Fig. 2). In the anhydrous pyrolysis with the Easy %R_o up to 2 the ratios
220 showed a small variation between 0.46 and 0.56, followed by a significant increase up to 0.82 at
221 Easy %R_o of 3.27. In general, in the hydrous pyrolysis the produced gases are drier than those in
222 the anhydrous experiments. The gas dryness in the pyrolysis of the Woodford Shale in this study
223 is comparable with that in Shuai et al. (2018) at the kerogen cracking stage, but lower at the oil

224 cracking stage. This is likely due to the different experimental conditions: for example, the
225 temperatures applied in the hydrous pyrolysis of Shuai et al. (2018) varied from 330 to 415 °C,
226 while in this study they changed from 310 to 370 °C. The natural gases from the Woodford Shale
227 reservoirs (Liu et al., 2019) are much drier than those in the artificial maturation experiments.

228 The total CO₂ and H₂S yields in the hydrous pyrolysis experiments, including those in the gases
229 and aqueous phases, increased from 1.17 to 2.14 and 0.71 to 2.33 mmol/g TOC, respectively. In
230 the anhydrous pyrolysis experiments their yields were much lower than those in the hydrous
231 pyrolysis experiments at similar thermal maturities (Table 1), as shown by Lewan (1997).
232 Measurable amounts of H₂ were produced in the pyrolysis of the Woodford Shale with slightly
233 higher yields in the anhydrous experiments compared with the hydrous conditions, which is similar
234 to the previous results of Woodford pyrolysis (Lewan, 1997).

235 4.2 C and H isotope compositions of hydrocarbon gases

236 In the hydrous conditions, δ¹³C of CH₄ (δ¹³C₁) showed a constant value of ~ -41‰ from the
237 immature to a main stage of the oil cracking (Easy %R_o: 1.67) (Fig. 3a). In the anhydrous
238 experiments, δ¹³C₁ first decreased slightly (-40.6 to -41.9‰) from the immature to a peak oil
239 window, then increased continually up to -35.6‰ at the highest maturity (Easy %R_o of 3.27). This
240 evolution trend in the anhydrous pyrolysis condition is consistent with the previous study on δ¹³C₁
241 values in the pyrolysis experiments with different kerogen types (Berner et al., 1995; Lorant et al.,
242 1998; Cramer, 2004; Dieckmann et al., 2006; Jia et al., 2014; He et al., 2018) or oil (Tian et al.,
243 2012). In the both hydrous and anhydrous experiments δ¹³C values of C₂H₆ and C₃H₈ (δ¹³C₂ and
244 δ¹³C₃) increased continually with the increasing thermal maturity from -38.9 to -26.8‰ and -35.9
245 to +5.8‰, respectively (Fig. 3a). The added water does not have a significant influence on the δ¹³C
246 evolution. This carbon isotopic characteristics were also observed in the immature, marine New

247 Albany Shale with the initial %R_o of 0.7 pyrolyzed in the maturity range of 1.3-1.9 (Easy %R_o)
248 (Gao et al., 2014) and Cretaceous coal with initial %R_o of 0.6 pyrolyzed in the maturity range of
249 1.7-2.3 (Ni et al., 2018). In the kerogen cracking stage, δ¹³C₁ values in this study were heavier than
250 those from the previous study (Shuai et al., 2018), but, in the oil cracking stage our δ¹³C₁ values
251 were much lower than their values at Easy %R_o of 2. The C₄ and C₅ alkanes showed increasing
252 δ¹³C values with the increasing maturities, especially after their cracking above Easy %R_o of 2
253 (Table 2).

254 In the hydrous pyrolysis experiments, δ²H values of HC gases were significantly lower than those
255 at the anhydrous conditions at similar maturities (Fig. 3b). δ²H_{C1} varied slightly between -292 and
256 -288‰ in the kerogen and oil cracking stages (Easy %R_o: 0.76 to 1.95) in the hydrous conditions,
257 but it increased significantly up to -148‰ in the anhydrous conditions at Easy %R_o up to 3.27. δ²H
258 values of ethane and propane firstly decreased and then increased in the hydrous pyrolysis
259 experiments, varying from -269 to -204‰ and -236 to -169‰, respectively. In the anhydrous
260 pyrolysis experiments, δ²H_{C2} and δ²H_{C3} values increased up to -51 and -33‰, respectively. δ²H
261 values of C₄ and C₅ showed similar evolution trends as C₂H₆ and C₃H₈. δ²H_{C1} values in this study
262 were heavier than those from the hydrous pyrolysis of Woodford Shale (Shuai et al., 2018) during
263 the kerogen and oil cracking stages (Fig. 3b).

264 4.3 Position-specific C isotopes of propane in pyrolysis gas

265 The position-specific (PS) carbon isotope deviation of propane ($\Delta C_{c-t} = \delta^{13}C_{cen} - \delta^{13}C_{ter}$) increased
266 continually with thermal maturity from 3.5 ± 1.5 to 6.3 ± 1.5 ‰ (hydrous) and 3.3 ± 1.5 to $30.6 \pm$
267 1.5 ‰ (anhydrous) (Table 3 and Fig. 4a). The evolution of the ΔC_{c-t} values from this study is
268 consistent with those from the Woodford Shale gases (Liu et al., 2019) and the Eagle Ford Shale
269 gases (Zhao et al., 2020) (Fig. 4a), but differs from those of the equilibrium model (Webb and

270 Miller, 2014). Similar ΔC_{c-t} trends with the maturity were observed in hydrous pyrolysis of the
271 Woodford kerogen (Piasecki et al., 2018) and n-C₂₅ cracking (Gilbert et al., 2019), but their values
272 have not been corrected for possible isotope fractionation during their measurements.

273 The $\delta^{13}C_{ter}$ of the propane remained nearly constant from the immature to oil window stages
274 (Easy %R_o: 1.2), then gradually increased in the late stage of oil cracking, and finally increased
275 significantly at the propane cracking stage (Easy %R_o > 2.2) (Fig. 4b). The $\delta^{13}C_{cen}$ increased
276 continually in the entire maturity range, especially in the wet-gas cracking stage. Assuming that
277 the $\delta^{13}C$ values of gas precursors of the Woodford Shale are the same as the value of the bulk
278 kerogen (-29‰) at the initial kerogen cracking stage, $\delta^{13}C_{ter}$ and $\delta^{13}C_{cen}$ values of propane
279 produced at the low maturation (Easy %R_o: ~ 0.8) could be estimated ~ -44 and ~ -35‰ in the
280 natural reservoir (150 °C), and ~ -37 and ~ -33.6‰ in the pyrolysis experiments (310 °C),
281 respectively, based on theoretical study of Tang et al. (2000). This theoretical calculation yields
282 more negative values (by ~ 7‰) than the observed $\delta^{13}C_{ter}$ values, but close to the $\delta^{13}C_{cen}$ of the
283 Woodford Shale gases at low maturity stage (Liu et al., 2019). They match the both values of the
284 pyrolysis gases at 310 °C (Fig. 4b).

285 5 Discussion

286 5.1 Experiments vs. theory on kinetics and isotope effects of Woodford Shale

287 5.1.1 Kinetics of gas generation and cracking

288 The C₁-C₃ gas yields in the kerogen cracking stage (Easy %R_o: 0.76 to 1.2) agree with the
289 predictions using the kinetic parameters (Table S1) from the pyrolysis of an immature New Albany
290 Shale (%R_o: 0.42) (Knauss et al., 1997). However, the predicted yields of C₁-C₃ by the kinetic
291 parameters from the pyrolysis of a mature Barnett Shale (%R_o: 1.15) (Xia, 2014) are significantly

292 lower than those from the Woodford and New Albany shales (Fig. 5), because mainly of a lower
293 gas potential in the mature source rock. During the oil cracking (Easy %R_o: 1.2 - 2), C₁-C₃ gas
294 yields in this study are compared with the calculations during the secondary cracking of oil to HC
295 gases (Tian et al., 2008) (Table S1 and Fig. 1). The oil used in Tian et al. (2008) is light (37 API
296 gravity and density of 0.84 g/cm³ at 20 °C) and enriched in short-chain alkanes, while heavy C₁₄₊
297 fractions account for 87% of the total oil production in the anhydrous pyrolysis of the Woodford
298 Shale (Shao et al., 2020). Meanwhile, kerogen cracking even at the oil cracking stage (Lorant and
299 Behar, 2002) can contribute to CH₄ yields in this study.

300 During the wet-gas cracking stage, the reaction rates (*k*) for C₃H₈ cracking from pure C₃H₈
301 cracking (Tian et al., 2008; Li et al., 2021) are approximately 1.5 - 2.2 times greater than those in
302 this study (Fig. 5) with the assumption described in Supplementary document S3. Continuing C₃H₈
303 production is a likely cause for the apparent lower C₃H₈ cracking rates in the Woodford Shale
304 pyrolysis, as HC gases can be generated from the condensation/aromatization reactions of
305 remaining kerogen, oil or residues at high maturities (e.g., Behar et al., 1997; Erdmann and
306 Horsfield, 2006; Mahlstedt and Horsfield, 2012). In the experiments of pure propane cracking at
307 450 °C for 72h (Easy %R_o: 2.66), the propane consumption accounts for 42 - 44% (Tian et al.,
308 2008; Li et al., 2021), compared with a value of 22% in the Woodford Shale pyrolysis. Assuming
309 the late-stage formed propane is not cracked, this indicates that additional ~ 20% of the theoretical
310 maximum propane yields are produced during the wet-gas cracking stage in the Woodford Shale
311 pyrolysis at 450 °C. Similarly at 470 °C (Easy %R_o: 3.07) ~ 18% of the maximum propane amounts
312 are generated. Therefore, propane production at the wet-gas cracking stage significantly influences
313 its cracking reaction rates, which likely affects the apparent kinetic isotope effects at the bulk and
314 position-specific level.

315 5.1.2 Isotope effects in gas generation and cracking

316 The bulk carbon isotope fractionation factors of C_3H_8 generated at 310 °C in our experiments of
317 the Woodford Shale agree well with the theoretical modeling values (k^*/k) (the asterisk denotes
318 ^{13}C) from n-alkane ($n \leq C_6$) cracking (Tang et al., 2000) based on the descriptions in
319 Supplementary document (Fig. S3). This suggests that the $\delta^{13}C$ of the Woodford kerogen can be
320 used as the $\delta^{13}C$ of propane precursors in the initial cracking stage and that the bond dissociation
321 occurs at a terminal site of propyl groups attached to alkanes. The C KIE at the terminal site is
322 larger than that at the central site (Fig. S4), which is also observed in the theoretical study on
323 propane generation from n- C_8 cracking (Ni et al., 2011). The magnitude of the position-specific C
324 KIE during propane cracking in the pyrolysis of the Woodford Shale is greater than those of the
325 pure propane cracking (Li et al., 2021), as seen for the bulk C KIE (Fig. S3). Continuing generation
326 of propane even at the wet-gas cracking stage is a significant factor controlling the position-
327 specific $\delta^{13}C$ values of propane from the Woodford Shale.

328 5.2 Natural vs. laboratory gas generation from Woodford Shale

329 Liu et al. (2019) reported gas, and bulk and position-specific isotopic compositions of the
330 unconventional Woodford Shale gases from the southwestern Arkoma Basin, Oklahoma. The
331 Woodford Shale used in this experimental pyrolysis study was collected ~ 80 km away at an
332 outcrop at the southern flank of the Arbuckle Uplift in the Ardmore Basin. The Woodford shale
333 was originally deposited in a vast stable shelf on the continental margin of North America during
334 Upper Devonian to Lower Mississippian. Therefore, the Woodford Shale sample used in this study
335 is expected to have very similar kerogen structures as the source rock for the gases in Liu et al.
336 (2019).

337 5.2.1 Gas compositions

338 As the most abundant non-hydrocarbon gas (up to ~ 45% in the pyrolysis gases), CO₂ is likely
339 sourced from carboxyl groups of the Woodford Shale with little carbonate, as suggested by their
340 $\delta^{13}\text{C}$ values (-27 to -31‰). The CO₂ yields are much higher in the hydrous pyrolysis. The oxidative
341 degradation of hydrocarbons with water (Seewald, 2001) could have contributed to the excess CO₂
342 as the C₂-C₅ yields are slightly lower and the overall gases are drier in the hydrous experiments
343 than those in the anhydrous experiments (Fig. 2). In natural Woodford Shale gases, the CO₂
344 concentrations are very low (< 1%) (Liu et al., 2019), due probably to the chemical reactions of
345 CO₂ with reservoir minerals (e.g., Sanna et al., 2014; Bickle et al., 2017).

346 The pyrolysis gases in this study contain measurable amounts of H₂ and H₂S, which have not been
347 detected in the Woodford shale gases. In the previous pyrolysis experiments, significant amounts
348 of H₂ sourced from organic-bounded hydrogen of kerogen were released (e.g., Behar et al., 1997;
349 Li et al., 2015), which could reduce hydrocarbon yields due to the competitive consumption of
350 hydrogen in the laboratory conditions. Typically, trace amounts (0.01 - 0.27%) of H₂ have been
351 found in natural gases such as in the Appalachian Basin (Jenden et al., 1993) and Ordos Basin (Liu
352 et al., 2015). There are some cases, where significant amounts of H₂ (35 - 98%) are accumulated
353 in reservoirs due to the inorganic processes (Coveney et al., 1987; Newell et al., 2007; Zgonnik,
354 2020). H₂ can also be generated by organic processes, including microbial activities and thermal
355 degradation of organic matter at high temperatures (Koyama, 1963; Conrad, 1996; Morita, 1999).
356 In sedimentary basins, H₂S in natural gases occurs mostly in marine carbonates gas reservoirs
357 because mainly of bacterial/thermochemical sulfate reduction and thermal cracking of S-rich
358 kerogen (e.g., Orr, 1977; Worden et al., 1995; Machel, 2001).

359 In the series of the pyrolysis experiments on the Woodford Shale, H₂S could be sourced from the
360 cracking of sulfur-containing organic compounds (e.g, thiols, sulfides) at 310 and 340 °C due to
361 the weak C-S bonds, and from inorganic sulfur species (e.g, pyrite) with increasing temperature
362 (e.g., Lewan and Kotarba, 2014; Ma et al., 2016). Based on the organic and inorganic sulfur
363 contents (0.7 and 1.7%, respectively) in the Woodford Shale (Craddock et al., 2018), a mass-
364 balance calculation suggests that the H₂S is mostly sourced from the organic species at the kerogen
365 cracking stage. With increasing maturity (temperature), pyrite (FeS₂) significantly contributes to
366 the formation of H₂S, up to ~ 60% in the anhydrous conditions at 430 °C in this study. The higher
367 yields of H₂S in the hydrous experiments compared with those in the anhydrous conditions (Table
368 1) indicate H in H₂S is originated from both organic compounds and the added water.

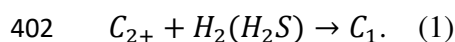
369 *5.2.1.1 Kinetic processes*

370 In order to investigate whether the kinetic parameters of gas generation obtained from
371 experimental studies can produce the dry gases observed in the natural Woodford Shale, the yields
372 of C₁-C₄ during the kerogen cracking stage are calculated based on the data of Knauss et al. (1997)
373 from 90 to 150 °C with a heating rate of 10 °C/m.y. during the rapid subsidence of the Arkoma
374 Basin (Byrnes and Lawyer, 1999). Assuming the maximum yields of methane and C₂-C₄ are twice
375 and 10 - 20% higher, respectively, than the measured yields (Tang et al., 1996; Tian et al., 2008),
376 the calculated gas dryness based on the kinetic model is much wetter than the observed values in
377 the both pyrolysis and natural Woodford Shale gases (0.35 - 0.4 at Easy %R_o of 0.5 - 1.2) (Fig. 2).
378 The assumed maximum yields of C₁-C₄ may not represent the natural conditions, because their
379 maximum yields change with a heating rate (e.g., Dieckmann et al., 2000; 2004). In natural
380 conditions with heating rates much slower than those of laboratory conditions, the gas yields could
381 go much higher, especially for methane, which could lead to a drier gas. A recent study focused

382 on the CH₄ yields in the low-temperature (60, 100 °C) pyrolysis of the New Albany Shale (Wei et
383 al., 2018) indicates that the generated gases could also be very dry in the laboratory conditions.
384 However, the very small amounts of methane produced at the low-temperature pyrolysis represent
385 only a small fraction of the potential gas generation in the kerogens most likely from the cracking
386 of methyl group with low activation energies (e.g., C-S, C-O bonds). However, vast majorities of
387 the gas generation in both pyrolysis and natural conditions are sourced from the cracking of C-C
388 bonds with much higher activation energies, requiring higher temperature or longer time for CH₄
389 generation. Assuming the same frequency factor for the cleavage of methyl groups, the logarithm
390 values of CH₄ generation rates in the cleavage of C-S and C-O bonds at 60 and 100 °C are ~ 7 - 8
391 orders of magnitude higher than those from C-C bonds, based on the dissociation energies of the
392 above bonds (Tang et al., 2000). This is consistent with the discrepancy that the low-temperature
393 CH₄ generation rates (Wei et al., 2018) are ~ 5 - 11 orders of magnitude greater than the
394 extrapolated values from the high-temperature experiments (Knauss et al., 1997). Therefore in
395 natural reservoirs with millions of years, the gases generated mainly from C-C bonds cracking
396 from different precursors are possibly wet, but they are still drier than those in laboratory
397 conditions.

398 5.2.1.2 Thermodynamic equilibrium

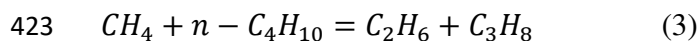
399 The high concentrations of C₂₊ gases and hydrogen-bearing gases (H₂ and H₂S) observed in the
400 pyrolysis gases can be examined in terms of thermodynamic reactions, rather than uni-directional
401 pyrolysis kinetics. The H₂ and H₂S would react with C₂₊ gases, leading to drier gases:



403 The equilibrium constants (*K*) of the reaction (1) under the ideal-gas assumption (Barin, 1995) are
404 in the range of 10⁴ - 10⁶ at our experimental conditions (310 - 480 °C), showing clearly that the

405 pyrolysis gases are out of thermodynamic equilibrium by 3 - 6 log units and that the reactions
406 should proceed to C₁-rich compositions with negligible concentrations of H₂ and H₂S. At a lower
407 temperature range for the generation of natural gases in sedimentary basins (100 - 200 °C), these
408 reactions drive further to C₁-rich and H₂ (and H₂S)-poor compositions, consistent with the gas
409 compositions of the Woodford shale gases (Liu et al., 2019). Hydrogenation-dehydrogenation
410 reactions of hydrocarbons, particularly of alkenes, are relatively fast and reversible (Seewald,
411 2001). Therefore, H₂ (and H₂S), which could be produced during kerogen maturation in natural
412 source rocks, are likely to be consumed by the above hydrogenation reactions. This is also
413 supported by the much lower H₂ yields in the closed-system pyrolysis, compared with those in the
414 open system pyrolysis of the same source rocks (Li et al., 2015, 2017). The Woodford Shale gases
415 have H/C values of 3.4 - 3.6 in the maturity range from 0.8-1.8%, while the ratios are lower (3 -
416 3.1) in the pyrolysis gas. If the all H₂ and H₂S are consumed by the hydrogenation reactions (1),
417 the ratios increase to 3.4-4, which are consistent with the values of the Woodford Shale gases (Fig.
418 S5).

419 The compositions of C₁-C₄ hydrocarbons from different origins (inclusions of igneous rocks,
420 volcanic gases, natural gases) have been debated (Giggenbach, 1980; Sugisaki and Nagamine,
421 1995; Tassi et al., 2007) in terms of the chemical reactions:



424 In select cases, the reaction (2) in volcanic gases and igneous inclusion gases appears to have
425 reached the equilibrium, yielding consistent temperatures with field observations (Sugisaki and

426 Nagamine, 1995; Tassi et al., 2007). Some investigators (e.g., Mango et al., 2009; Cesar et al.,
427 2021) also discussed equilibrium reactions of hydrocarbon systems in sedimentary basins.

428 We have compared gas products from the pyrolysis experiments in this study and the natural gases
429 from the Woodford Shale in Liu et al. (2019) with thermodynamic equilibrium constants (K) of
430 the reactions (2) and (3), calculated under the ideal-gas assumption (Barin, 1995) (Fig. 6). The
431 pyrolysis gases in this study appear to be clearly out of equilibrium, moving in a direction away
432 from the equilibrium with increasing temperature (310 to 480 °C), as noticed before for the results
433 from other pyrolysis experiments (Sugisaki and Nagamine, 1995). Apparently, the chemical
434 reactions among C₁-C₄ gases are slow, compared with pyrolysis reactions during kerogen
435 maturation within typical experimental durations.

436 The data of the Woodford Shale gases (Liu et al., 2019) shows that at the low temperatures (140 °C),
437 they are close to the equilibrium of the reaction (2) (Fig. 6), considering likely combined
438 uncertainty (ca. 0.2 log unit) of the thermodynamic and analytical data. Then, they start to deviate
439 with increasing temperature to 160°C. Uncertainty in the estimated peak temperatures of the
440 Woodford Shale ($\pm 10 - 20$ °C) based on their kerogen maturity (Liu et al., 2019), would not change
441 the above observations. A similar pattern is also observed for the reaction (3), but the
442 thermodynamic data for nC₄ appears to have larger uncertainty.

443 Based on a geothermal gradient of 25 - 30 °C/km in the Arkoma Basin (Byrnes and Lawyer, 1999),
444 the Woodford shales in the western Arkoma Basin in Liu et al. (2019) had most likely been buried
445 to 4.5 - 7 km deep at its peak maturation, corresponding to hydrostatic pressures of 45 - 70 MPa.
446 At this estimated T-P range the gases in the Woodford Shale reservoir do not behave as ideal gases:
447 the compressibility (or fugacity coefficient) of C₁ is most likely greater than unity, while those of
448 other minor gases (C₂-C₄) are smaller than unity (Danesh, 1998). These non-ideal behaviors of the

449 gases likely result in lower logK values of the reaction (2) by 0.2 - 0.3, compared to the ideal-gas
450 values, bringing those of the Woodford Shale gases closer to the predicted equilibrium values (Fig.
451 6). During the generation of the Woodford Shale gases, the pressure within the Woodford Shale
452 most likely increased above the hydrostatic pressure. This overpressure, which can reach 1.5 times
453 the hydrostatic pressures in shales due to kerogen cracking to gases (Tingay et al., 2013), would
454 further lower the logK values of the reaction (2), closer to the values of the Woodford Shale gases.
455 We have not considered possible non-ideal mixing of the natural gases under the burial conditions.
456 Expulsion of early wet gases and subsequent accumulation of late-stage dry gases likely increase,
457 rather than decrease, the logK values. These considerations of chemical equilibrium among C₁-C₄
458 gases suggest that the Woodford Shale gases might have approached close to chemical equilibrium
459 at their peak temperatures (140 - 190°C) for 10 - 20 m.y. soon after the deposition (Byrnes and
460 Lawyer, 1999). However, the rates and mechanisms of chemical reactions among C₁-C₄ gases
461 under sedimentary conditions are currently poorly understood.

462 5.2.2 Bulk isotopes of hydrocarbon gases

463 In the earliest stage of the kerogen cracking in this study (Easy %R_o = 0.76 at 310 °C), the measured
464 δ¹³C values of the generated C₁-C₃ agree well with those calculated from the theoretical studies of
465 C KIE during radicals cleavage from n-alkane (Tang et al., 2000), assuming that precursors for C₁-
466 C₃ have the same δ¹³C value as the kerogen (-29‰). However, similar calculations for the
467 Woodford Shale gases at the lowest maturation (Easy %R_o = ~ 0.8 at 140 °C) yield δ¹³C values
468 much lower than those of the shale gases. In fact, the δ¹³C values of C₁ and C₃ from the pyrolysis
469 and the natural gases are very similar to each other at the low maturity despite at the very different
470 temperatures (140 vs. 310 °C) (Fig. 3a). During the maturation of kerogen in natural settings, HC
471 gases are generated from the cracking of C-S bonds first, rather than C-C, because the former

472 bonds have much lower dissociation energy. The C KIE associated with the C-S breaking for CH₃-
473 radical is much smaller (~ 0.99) than those of C-C (~ 0.97) at 140 °C (Tang et al., 2000). Therefore,
474 CH₄ produced from C-S cracking of the Woodford kerogen at low maturity would have a δ¹³C₁
475 value of ~ -40‰, which is close to the observed values of the Woodford Shale gases (~ -42‰).
476 The cracking of C-C bonds of the Woodford kerogen could also be catalyzed by the formation of
477 S radicals in the early hydrocarbon generation (Lewan, 1998), but C KIE associated with the S-
478 catalyzed C-C cracking is not known. With increasing maturity, C-C cracking increasingly
479 produces C₁-C₃ with larger C KIE and lower δ¹³C values, consistent with the observations of the
480 Woodford shale gases (Fig. S6). The kinetic Monte Carlo (kMC) simulations of pure n-alkanes
481 (Peterson et al., 2018) also produced similar decreasing and increasing trends in δ¹³C values of C₁-
482 C₃ with maturity, but the δ¹³C₁ values were much lower than those of the Woodford shale gases.

483 5.2.2.1 Hydrogen sources of C₁-C₃

484 To interpret the δ²H values of C₁-C₃ produced from the Woodford kerogen in the natural and
485 pyrolysis conditions, we examine three different models (H KIE for capping H, H-exchange for
486 capping H, full exchange with water). In the gas generation, we need to model how C₁-C₃ alkyl
487 radicals, which are cleaved from the kerogen and other precursors, inherit the last H (capping
488 hydrogen) from other H-bearing compounds. We assume that their precursors have a δ²H value of
489 -100‰ based on those of the type II kerogen (Schimmelmann et al., 1999). Hydrogen KIE during
490 the cracking of -CH₃, -CH₂CH₃ and -CH₂CH₂CH₃ radicals are calculated from n-C₈ cracking (Ni
491 et al., 2011). Dong et al. (2021) assumed that the capping H for alkyl radicals was abstracted from
492 the same precursors for hydrocarbon gas generation with the primary H KIE from Gray et al.
493 (1971), which is described with an A^{*}/A value of 1.0745 and ΔE_a (= E_a^{*} - E_a, dissociation energy
494 difference) of 5409.1 J/mol.

495 The capping H for the alkyl radicals could come from other H-bearing gases. The measurable
496 amounts of H₂ and H₂S were generated in the pyrolysis experiments of the Woodford Shale. The
497 δ²H values of H₂ (Table 2) appear very close to isotopic equilibrium with the water at the
498 experimental temperatures (310 - 480 °C), suggesting that the H₂, which was most likely produced
499 from thermal cracking of kerogen C-H bonds, exchanged with the water, reaching the isotopic
500 equilibrium, rather than controlled by H KIE during breaking of C-H bonds. The measured δ²H
501 values of H₂S do not represent the source or formation conditions, because the H₂S continued
502 undergoing retrograde isotopic exchange with the water during the cooling after the experiments.
503 It is assumed that the H₂ and H₂S are both generated in isotopic equilibrium with the water and
504 that the alkyl radicals acquire the capping H from these gases. The concentrations of H₂ and H₂S
505 in natural gases are usually low or under the detecting limit, but they may act as intermediate H-
506 reservoirs for the capping H. Based on the estimated δ²H values of Woodford formation water (-
507 30‰) (Liu et al., 2019), we calculate δ²H values of the capping H for alkyl radicals (Thiagarajan
508 et al., 2020; Turner et al., 2021). Another scenario is that the δ²H values of C₁-C₃ were controlled
509 by H isotope equilibration with the excess water during and/or after the gas generation
510 (Thiagarajan et al., 2020; Turner et al., 2021).

511 When the capping H is sourced from organic compounds with the large H KIE, the predicted δ²H
512 values of C₁-C₃ are generally more negative than those from the natural shale gases (Liu et al.,
513 2019) (Fig. 7), but generally agree with those of the pyrolysis gases. Assuming the capping H is
514 in isotopic equilibrium with the water during gas generation, the predicted δ²H values are much
515 more positive than those of the pyrolysis C₁-C₃ in the hydrous (310 - 370 °C) and anhydrous
516 conditions (310 - 400 °C), but the two sets of data may become close above 400 °C in the anhydrous
517 experiments. The agreement with the natural shale gases are much better than the H KIE model

518 (Fig. 7). The H full exchange model between water and C₁-C₃ yields the $\delta^2\text{H}_{\text{C}_1}$ values close to the
519 values of the natural methane, but the modelled $\delta^2\text{H}$ values of C₂-C₃ are more positive than those
520 of the both natural and pyrolysis gases below 400 °C (Fig. 7). The $\delta^2\text{H}$ values of C₁-C₃ from the
521 hydrous experiments are lower than those of the anhydrous experiments, but the latter system also
522 contains small amounts of water produced during the kerogen cracking with unknown $\delta^2\text{H}$ values.

523 Overall, the results from these three models suggest that in the pyrolysis conditions the capping H
524 is mainly from C-H bonds cracking with large KIE or experiences H isotope exchange with the
525 water with increasing temperature, consistent with the modeling results for clumped $\Delta^{12}\text{CH}_2\text{D}_2$
526 produced from n-C₁₈ pyrolysis (Dong et al., 2021). In the natural conditions, $\delta^2\text{H}$ values are more
527 consistent with the models for partial to full isotope exchange with water. These observations
528 somewhat contradict the results from the experimental studies with water of elevated $\delta^2\text{H}$ values,
529 which show that the water-derived hydrogen has limited influence on methane generation in low
530 temperature conditions, but at high temperature water-derived hydrogen to C₁-C₃ accounts for 10's
531 of % (Wei et al., 2018). This inconsistency is likely due to the reason that the effect of hydrogen
532 exchange between hydrocarbon gases and water is insignificant at the short experimental
533 conditions (< 5 years), compared with that in natural reservoirs (millions of years).

534 5.2.2.2 Kinetic vs. equilibrium control of carbon and hydrogen isotopes

535 Several investigators (James, 1983; Thiagarajan et al., 2020) also argued that carbon isotope
536 equilibria among C₁-C₅ might have been attained in reservoir conditions for some matured natural
537 gases. Following the discussions above on the attainment of chemical equilibria of C₁-C₄ gases
538 and the isotope exchange of the capping H, possible attainment of carbon and hydrogen isotope
539 equilibria among C₁-nC₄ gases is examined in more detail (Fig. 8). The differences in the isotopic
540 compositions of several hydrocarbon pairs ($\delta^{13}\text{C}$: C₂-C₁, C₃-C₁, C₃-C₂, and C₄-C₂; $\delta^2\text{H}$: C₂-C₁, C₃-

541 C₁) from the Woodford pyrolysis gases show that they are close to equilibrium values at 300-350
542 °C, but start to deviate significantly with increasing temperature. With increasing temperature,
543 many isotope pairs approach much closer to those controlled by C and H kinetic isotope effect
544 based on the gas generation from n-C₈ cracking (Ni et al., 2011). Similar to the patterns of the
545 molecular compositions of the gases (Fig. 6), all these δ¹³C and δ²H patterns of the pyrolysis gases
546 appear to be controlled by the kinetics of thermal cracking. The δ¹³C and δ²H values of the
547 Woodford Shale gases show somewhat more complex patterns, although tightly aligned together.
548 Differences in the δ¹³C and δ²H values of the hydrocarbons pairs all increase with temperature
549 between 140 and 160/170 °C, but then decrease with temperature to 190 °C. The initial increase
550 below 160/170 °C is particularly pronounced for C₂-C₁ and C₃-C₁ pairs and this is due largely to
551 the elevated δ¹³C₁ and δ²H_{C1} values (Fig. S6) from C-S/C-O cracking at the early kerogen
552 maturation stage as discussed above. Above 160/170 °C, the δ¹³C differences of C₂-C₁ and δ²H
553 differences of C₃-C₁ and C₂-C₁ appear to be close to equilibrium values within uncertainty of
554 theoretical calculations (Thiagarajan et al., 2020; Polyakov and Horita, 2021), but the other pairs
555 (δ¹³C: C₃-C₁, C₃-C₂, C₄-C₂; δ²H: C₃-C₂, C₄-C₂) show measurable discrepancies, compared with the
556 equilibrium fractionation. Data of the Woodford Shale gases above 160/170 °C are plotted between
557 the equilibrium and kinetic fractionation values (Fig. 8).

558 The half-life of H-isotope exchange between C₁ and water ranges from < 1 m.y. (190 °C) to 10's
559 of m.y. (140°C) (Wang et al., 2018). The half-life for C₂₊ hydrocarbons is likely shorter than that
560 for C₁ as Reeves et al. (2012) showed that hydrogen isotope exchange between water and various
561 light hydrocarbons can proceed via hydrogenation-dehydrogenation of alkanes and their alkene
562 counterparts in the order: C₄-C₅>C₃≥C₂>C₁. It is also expected that hydrogen isotope exchange
563 among C₁-C₄ proceeds faster than C isotope exchange through various hydrogenation-hydrolysis

564 reactions, possibly catalyzed by the mineral surface. Within these contexts, it is somewhat
565 surprising that the $\delta^2\text{H}$ differences of $\text{C}_3\text{-C}_1$ and $\text{C}_2\text{-C}_1$ pairs in the Woodford Shale gases are closer
566 to their isotopic equilibrium than those of $\text{C}_3\text{-C}_2$ and $\text{C}_4\text{-C}_2$ and that $\delta^{13}\text{C}$ differences of the $\text{C}_2\text{-C}_1$
567 pair, but not others, show an apparent isotope equilibrium at the highest temperature (190 °C).

568 Overall, the isotopic patterns of the pairs (Fig. 8) could be interpreted that at the low maturity
569 (<160/170 °C), kinetic isotope effects including CH_4 generation from C-S/C-O cracking dominate,
570 but with increasing maturity (>160/170 °C) at the peak burial period of 10 - 20 m.y., they started
571 shifting toward the equilibrium isotope fractionation, controlled by (mineral-catalyzed) chemical
572 reactions among HC, water, and other gases. Better understanding of the mechanisms and rates of
573 chemical reactions involving HC gases under sedimentary conditions is needed, along with more
574 accurate data on thermodynamics and isotope effects (Fig. 6 and 8).

575 5.2.3 Comparison of position-specific C isotopes of propane with kMC simulations

576 All the $\delta^{13}\text{C}_{\text{cen}}$ and $\delta^{13}\text{C}_{\text{ter}}$ data of the Woodford natural and pyrolysis gases, and others available
577 from the literature are shown (Fig. 9a). The $\delta^{13}\text{C}_{\text{ter}}$ and $\delta^{13}\text{C}_{\text{cen}}$ values of propane from natural
578 reservoirs and pyrolysis experiments in the literature (Suda et al., 2017; Piasecki et al., 2018;
579 Gilbert et al., 2019; Zhang et al., 2022) are not properly corrected for position-specific (PS) isotope
580 fractionation associated with HR-IRMS and GC-Pyrolysis-GC IRMS analysis. The values of
581 Piasecki et al. (2018) with HR-IRMS are corrected, assuming their Eagle Ford data are similar to
582 those by Zhao et al. (2020). The results of Suda et al. (2017), Gilbert et al. (2019) and Zhang et al.
583 (2022) with GC-Pyrolysis-GC IRMS are corrected based on the PS fractionation factors
584 determined in our study (Supplementary document S2, Fig. S1). However, these corrected values
585 of the literature data may have large uncertainty.

586 Peterson et al. (2018) conducted kinetic Monte Carlo (kMC) simulations on $\delta^{13}\text{C}_{\text{ter}}$ and $\delta^{13}\text{C}_{\text{cen}}$
587 values during the cracking of model alkane compounds ($n = 4 - 40$). They assumed: (a) ^{13}C is
588 randomly distributed in the substrates, (b) the KIE of C-C breaking is -30% , and (c) no
589 secondary/tertiary KIE occurs during the cracking. Xie et al. (2022) further improved the kMC
590 simulations of position-specific $\delta^{13}\text{C}$ values of propane from the thermal cracking at $227\text{ }^\circ\text{C}$, (a)
591 using a model compound of type I kerogen with multiple types of bonds (e.g., C-C bonds in
592 aliphatic and aromatic groups, C-S, C-O) and (b) considering secondary/tertiary KIE in gas
593 generation. Xie et al. (2022) considered two reaction schemes: radicals are formed by a single
594 bond dissociation and subsequently capped with a H atom (scheme A) and radicals generated by
595 the homolytic cleavage experience the reactions of β -scission, radical isomerization, H-abstraction,
596 and the radical recombination (scheme B). We have normalized their simulation results (Peterson
597 et al., 2018; Xie et al., 2022) with the initial $\delta^{13}\text{C}$ value of organic precursors which is the same as
598 that of the Woodford Shale (-29%).

599 At the early stages of C_3H_8 generation, the position-specific $\delta^{13}\text{C}$ values from the two kMC
600 simulations (Peterson et al., 2018; Xie et al., 2022) differ. The $\delta^{13}\text{C}_{\text{cen}}$ values of Peterson et al.
601 (2018) are greater than those of Xie et al. (2022), because the former study did not consider the
602 secondary C KIE in the cracking of propyl radicals. The $\delta^{13}\text{C}_{\text{ter}}$ values of Xie et al. (2022) are much
603 greater than those of Peterson et al. (2018), due most likely to small C KIE in the cracking of
604 propyl radicals from C-S/C-O bonds at early kerogen cracking stage. The results of Peterson et al.
605 (2018) and Xie et al. (2022) scheme A both show similar rapid increases in the both $\delta^{13}\text{C}_{\text{ter}}$ and
606 $\delta^{13}\text{C}_{\text{cen}}$ values in late stages of propane generation. The scheme B of Xie et al. (2022) shows much
607 smaller increases in the $\delta^{13}\text{C}_{\text{ter}}$ and $\delta^{13}\text{C}_{\text{cen}}$ values. The C_3H_8 produced in the pyrolysis experiments
608 of $n\text{C}_{25}$ at $500\text{ }^\circ\text{C}$ from 0.5 to 5 h (Gilbert et al., 2019) also shows increasing $\delta^{13}\text{C}_{\text{ter}}$ and $\delta^{13}\text{C}_{\text{cen}}$

609 trends similar to those of the kMC simulations. The kinetic parameters (Li et al., 2021) suggest
610 that 8 to 58% of the C₃H₈ produced in the pyrolysis of nC₂₅ at 500 °C from 0.5 to 5 h is consumed
611 by cracking, but C₃H₈ cracking at the wet-gas cracking stage also increases δ¹³C_{ter} and δ¹³C_{cen}
612 values with a similar slope in Fig. 9a (Li et al., 2021).

613 The δ¹³C_{ter} and δ¹³C_{cen} values of the natural Woodford Shale propane are slightly (~ 1 and 3‰,
614 respectively) lower than those from the early-stage propane of the pyrolysis experiments in this
615 study, reflecting the different temperatures: 140 - 190 vs. 310 - 360 °C, respectively. During the
616 pyrolysis of the Woodford Shale, the δ¹³C_{cen} values increased more rapidly than δ¹³C_{ter}, resulting
617 in a significant increase in ΔC_{c-t} values. These data are very consistent with the kMC scheme A
618 simulation of the model type I kerogen compound (Xie et al., 2022). The kMC simulations of C₃H₈
619 production from nC₂₀/nC₄₀ (Peterson et al., 2018) have large offsets from our pyrolysis data and
620 Scheme A simulation (Xie et al., 2022) as discussed above. The results from the pyrolysis of
621 another type II kerogen (Zhang et al., 2022) also show a very similar pattern with the off-set
622 stemming from the different δ¹³C of kerogen (-25.3‰). Overall, the kMC simulations of the simple
623 pyrolysis scheme A (no β-scission, radical isomerization, H-abstraction, and the radical
624 recombination) (Xie et al., 2022) produced the results very similar to those of the laboratory
625 pyrolysis of kerogens in this study and Zhang et al. (2022).

626 Considering much slower C₃H₈ cracking reaction rates in the Woodford Shale pyrolysis compared
627 with that in the pure C₃H₈ cracking (Li et al., 2021), we estimate that significant amounts of C₃H₈
628 were produced in the wet-gas cracking stage (up to ~ 30% of the theoretical maximum propane
629 yields) with heavy δ¹³C values at the central and terminal sites. A isotope balance calculations
630 based on the yields and δ¹³C₃ between the two studies implies that the average δ¹³C of the propane
631 produced at the wet-gas cracking could have ~ -17, ~ -24.8, and ~ 1.5‰ for bulk, terminal and

632 central sites, respectively, at 450 °C, possibly from the condensation reactions in the remaining
633 Woodford kerogen or other thermally stable organic compounds.

634 The hydrous and anhydrous pyrolysis of the Woodford kerogen (Lewan, 1997) produced a wide
635 distribution of n-alkanes (C₅-C₃₇) with certain amounts of branched alkanes. Therefore, the propyl
636 groups could also be generated from the cracking of isoprenoid structures (Piasecki et al., 2016).
637 However, the small C KIE observed between the bulk $\delta^{13}\text{C}$ (-29 ‰) of the kerogen and $\delta^{13}\text{C}_{\text{cen}}$
638 values (-33 to -30‰) of the early-stage propane from the cracking of the Woodford Shale (Fig. 9a)
639 suggest that the contribution of isoprenoid structures to propane is limited. The results from a
640 similar hydrous pyrolysis of a Woodford shale (Piasecki et al., 2018) show that $\delta^{13}\text{C}_{\text{ter}}$ and $\delta^{13}\text{C}_{\text{cen}}$
641 values are quite different from other natural and pyrolysis gases, and our corrections of the isotope
642 fractionation to their data may not be adequate.

643 5.3 Position-specific C and H isotopes of propane from natural reservoirs

644 The results of position-specific isotope values of propane from natural gases of different sources
645 shows that most of thermogenic gases (Woodford, Eagle Ford, Southwest Ontario, Michigan,
646 Carnarvon, Tarim) (Liu et al., 2019; Gilbert et al., 2019; Zhao et al., 2020; Zhang et al., 2022)
647 cluster along a common linear trend with positive $\delta^{13}\text{C}_{\text{ter}} - \delta^{13}\text{C}_{\text{cen}}$ correlation (Fig. 9a). With a few
648 exceptions, the $\delta^{13}\text{C}_{\text{cen}}$ is greater than the $\delta^{13}\text{C}_{\text{ter}}$ and the $\Delta\text{C}_{\text{c-t}}$ values generally increase with
649 increasing maturity. The Tarim gases have the highest $\delta^{13}\text{C}_{\text{ter}} - \delta^{13}\text{C}_{\text{cen}}$ values among the natural
650 gases (excluding Michigan and Carnarvon), following the trend of the wet-gas cracking, due to
651 their high maturities (%R_o: 1 - 2.3). The kMC scheme A simulation of a type I kerogen compound
652 (Xie et al., 2022) generally follows the natural trend, while the scheme B produce much smaller
653 isotopic variations with similar $\delta^{13}\text{C}_{\text{ter}}$ and $\delta^{13}\text{C}_{\text{cen}}$ values at the very high maturity. The limited
654 database of $\delta^{13}\text{C}_{\text{ter}}$ and $\delta^{13}\text{C}_{\text{cen}}$ values of the natural and pyrolysis gases, and the kMC simulation

655 (Xie et al., 2022) indicate: (a) the isotopic structures of natural propane precursors within three
656 types kerogens (lacustrine, marine source rocks and coal) are relatively similar to each other, (b)
657 ^{13}C distributes randomly within propane precursors, although continuing cracking of the
658 precursors to produce various HC's would obscure possible non-random distributions (Peterson et
659 al., 2018), (c) the cracking of propyl radicals occurs predominantly at the terminal site, (d)
660 reactions (β -scission, radical isomerization, H-abstraction, and radical recombination) following
661 the cracking of propyl radicals may be limited.

662 The two samples from the U. Devonian Antrim deposit in Michigan Basin show very elevated
663 $\delta^{13}\text{C}_{\text{cen}}$ values, due most likely to biodegradation (Gilbert et al., 2019). Transport processes such
664 as diffusion are unlikely to cause large isotope fractionation (Fig. 9a) (Piasecki et al., 2016). A gas
665 sample of possible abiogenic origin from a terrestrial serpentine-hosted hot spring (Suda et al.,
666 2017) shows light $\delta^{13}\text{C}_3$ with similar $\delta^{13}\text{C}_{\text{ter}}$ and $\delta^{13}\text{C}_{\text{cen}}$ values. Thermogenic processes, including
667 wet gas cracking, and biodegradation activities appear to be the significant factors in controlling
668 the terminal and central ^{13}C of propane.

669 A summary on the reported position-specific $\delta^2\text{H}$ of propane from the natural gas samples and the
670 pyrolysis gases (Liu et al., 2018, 2019; Xie et al., 2020; Zhao et al., 2020) show that the $\delta^2\text{H}_{\text{cen}}$ is
671 lower by $\sim 100\%$ than the $\delta^2\text{H}_{\text{ter}}$ in an early to middle stage of kerogen cracking ($\%R_o < \sim 1$) (Fig.
672 9b). Then, the $\delta^2\text{H}_{\text{cen}}$ values rapidly increase with maturation, while the $\delta^2\text{H}_{\text{ter}}$ increases gradually,
673 resulting in the positive $\Delta\text{H}_{\text{c-t}}$ values. The rapid increase in the $\delta^2\text{H}_{\text{cen}}$ of the Woodford Shale gases
674 ($\%R_o$: 0.8 - 1.7) was interpreted as the result of progressive H-isotope exchange with the shale
675 water (Liu et al., 2019). The C_3H_8 generated from the laboratory pyrolysis of a Woodford Shale
676 (Xie et al., 2020) show a similar evolutionary trend in $\delta^2\text{H}_{\text{cen}}$ and $\delta^2\text{H}_{\text{ter}}$ values, but with large off-
677 sets to lower values. They interpreted that the very low $\Delta\text{H}_{\text{c-t}}$ values (-80 to -100%) observed from

678 a Potiguar natural gas and the Woodford pyrolysis gases (Piasecki et al., 2018) are due to the
679 cracking of isoprenoid groups, rather than linear alkyl groups at early stages of the maturation.
680 However, the ΔC_{c-t} from the same set of the Woodford pyrolysis gases have very positive values
681 (20 - 26‰) (Fig. 9a), indicating that propyl radicals mainly cleaved at the terminal site, rather than
682 at the central site from the branched chains (e.g., isoprenoids). Combined with the ΔC_{c-t} and ΔH_{c-t}
683 values of propane in the Woodford Shale pyrolysis, we interpret that the δ^2H values at the terminal
684 sites of propane precursors in the kerogen are much heavier than those at the central sites. Thermal
685 cracking and subsequent H-isotope exchange appear to modify δ^2H_{cen} values of propane more
686 significantly than δ^2H_{ter} values (Liu et al., 2019; Xie et al., 2020). The natural gas samples from
687 the U.S. Gulf of Mexico (GOM) Basin show very elevated δ^2H_{cen} values, which were interpreted
688 to have experienced biodegradation (Xie et al., 2020), similar to the very elevated $\delta^{13}C_{cen}$ values
689 (Fig. 9a). However, the effect of biodegradation on PS δ^2H values needs to be investigated by
690 laboratory experiments. Compared with the discussions of chemical equilibrium in the natural
691 Woodford Shale gases and pyrolysis gases above, the position-specific C and H isotopes of
692 propane provide more direct and reliable evidence on the non-equilibrium state at the
693 intramolecular level.

694 6 Conclusions

695 The detailed comparisons of the pyrolysis and natural shale gases from the same source rock of a
696 type II kerogen, the Upper Devonian-Lower Mississippian Woodford Shale in Oklahoma, show
697 that the gases generated from the laboratory pyrolysis experiments are much wetter with elevated
698 contents of CO_2 , H_2S , and H_2 , compared to the natural Woodford gases, and that the kinetic data
699 obtained from laboratory pyrolysis experiments are not able to reproduce the gas dryness observed
700 in the natural shale reservoirs. The Woodford pyrolysis gases show that the both gaseous and

701 isotopic compositions of C₁-C₅ are controlled largely by the kinetic processes. The thermodynamic
702 equilibrium reactions are the important factors driving the wet to very dry gases in natural
703 reservoirs, including non-hydrocarbon gases, possibly approaching the chemical and isotopic
704 equilibrium at the deepest burial. The isotopic data of the Woodford Shale gases indicate that they
705 are influenced largely by kinetic processes at the low maturation, but appear to approach toward
706 the isotope equilibrium at the highest burial temperature (190 °C). Our modeling suggests that the
707 capping H for C₁-C₃ gases in the Woodford Shale had likely experienced H isotope exchange with
708 the formation water in the shale, but the pyrolysis gases abstracted H from the kerogen with the
709 large H KIE.

710 The position-specific isotopic data of propane in the natural and pyrolysis gases collected from
711 this study and the literatures presents a first-order framework for our understanding of the PS
712 isotope compositions. The common linear trend in the $\delta^{13}\text{C}_{\text{cen}} - \delta^{13}\text{C}_{\text{ter}}$ relation with increasing $\Delta\text{C}_{\text{c-}}$
713 t values with maturity indicate that the intramolecular isotopic structures of propane precursors
714 within kerogens are similar to each other. The increasing $\delta^{13}\text{C}_{\text{cen}}$ and $\delta^{13}\text{C}_{\text{ter}}$ values during the wet-
715 gas cracking stage is likely due to the generation of propane with relative heavy ¹³C from thermally
716 stable organic compounds. A compilation of PS $\delta^2\text{H}$ values of propane shows that propane
717 produced in the early stages has large negative $\Delta\text{H}_{\text{c-t}}$ values and that $\delta^2\text{H}_{\text{cen}}$ values increase
718 significantly with maturation due to isotopic exchange with water and possible other causes. The
719 effects of diffusion and other migration processes on the PS isotopes are probably limited.

720 In shallow gas deposits, biodegradation can increase $\delta^{13}\text{C}_{\text{cen}}$ and $\delta^2\text{H}_{\text{cen}}$ values significantly. This
721 study demonstrates that PS isotope analysis of propane can contribute to our understanding of
722 various geological processes, such as biodegradation, H exchange, and others. The information of
723 position-specific isotopic compositions of propane has shown a potential for tracing the source and

724 maturity of natural gases, identifying microbial oxidation activities in natural reservoirs. Further
725 works on the position-specific isotope fractionation of propane, integrated with other innovative
726 approaches (clumped methane and ethane, theoretical calculations, and numerical simulations) are
727 expected to provide a better understanding of light hydrocarbons in nature.

728

729 Acknowledgements

730 We thank four reviewers for their constructive comments that improve this manuscript greatly.
731 Financial support was provided by U. S. Department of Energy Geosciences program (DE-
732 SC0016271).

733

734 Reference

- 735 Barin I. (1995) Thermodynamic data of pure substance. Third edition, VCH, Weinheim, Germany.
- 736 Behar F., Vandenbroucke M., Tang Y., Marquis F., Espitalié J. (1997) Thermal cracking of
737 kerogen in open and closed systems: determination of kinetic parameters and stoichiometric
738 coefficients for oil and gas generation. *Org. Geochem.* **26**, 321-339.
- 739 Bernard B. B., Brooks J. M., Sackett W. M. (1976) Natural gas seepage in the Gulf of Mexico.
740 *Earth Planet. Sci. Lett.* **31**, 48-54.
- 741 Berner U., Faber E., Scheeder G., Panten D. (1995) Primary cracking of algal and landplant
742 kerogens: kinetic models of isotope variations in methane, ethane and propane. *Chem. Geol.*
743 **126**, 233-245.
- 744 Bickle M., Kampman N., Chapman H., Ballentine C., Dubacq B., Galy A., Sirikitputtisak T.,
745 Warr O., Wigley M., Zhou Z. (2017) Rapid reactions between CO₂, brine and silicate
746 minerals during geological carbon storage: Modelling based on a field CO₂ injection
747 experiment. *Chem. Geol.* **468**. 17-31.

748 Byrnes A. P., Lawyer G. (1999) Burial, maturation, and petroleum generation history of the
749 Arkoma Basin and Ouachita Foldbelt, Oklahoma and Arkansas. *Nat. Resour. Res.* **8**, 3-26.

750 Cesar J., Mayer B., Deblonde C., Mort A., Ardakani O. H. (2021) Alternative indicators to assess
751 the distribution characteristics of methane, ethane, and propane derived from petroleum in
752 the Montney Formation, Western Canada. *Fuel* 294, 120524.

753 Chung H. M., Gormly J. R., Squires R. M. (1988) Origin of gaseous hydrocarbons in subsurface
754 environments: theoretical considerations of carbon isotope distribution. *Chem. Geol.* **71**, 97-
755 103.

756 Conrad R. (1996) Soil microorganisms as controllers of atmospheric trace gases (H₂, CO, CH₄,
757 OCS, N₂O, and NO). *Microbiol. Rev.* **60**, 609-640.

758 Coveney J. R. M., Goebel E. D., Zeller E. J., Dreschhoff G. A. M., Angino E. E. (1987)
759 Serpentinization and the origin of hydrogen gas in Kansas (USA). *AAPG Bull.* **71**, 39-48.

760 Craddock P. R., Bake K. D., Pomerantz A. E. (2018) Chemical, molecular, and microstructure
761 evolution of kerogen during thermal maturation: Case study from the Woodford Shale of
762 Oklahoma. *Energy Fuels* **32**, 4859-4872.

763 Cramer B. (2004) Methane generation from coal during open system pyrolysis investigated by
764 isotope specific, Gaussian distributed reaction kinetics. *Org. Geochem.* **35**, 379-392.

765 Danesh A. (1998) PVT and Phase Behaviour of Petroleum Reservoir Fluids. Elsevier Science,
766 Oxford.

767 Dieckmann V., Horsfield B., Schenk H. J. (2000) Heating rate dependency of petroleum
768 forming reactions: implications for compositional kinetic predictions. *Org. Geochem.*
769 **31**, 1333-1348.

770 Dieckmann V., Fowler M., Horsfield B. (2004) Predicting the composition of natural gas generated
771 by the Duvernay Formation (Western Canada sedimentary basin) using a compositional kinetic
772 approach. *Org. Geochem.* **35**, 845-862.

773 Dieckmann V., Ondrak R., Cramer B., Horsfield B. (2006) Deep basin gas: New insights from
774 kinetic modelling and isotopic fractionation in deep-formed gas precursors. *Mar. Pet. Geol.*
775 **23**, 183-199.

776 Dong G. N., Xie H., Formolo M., Lawson M., Sessions A., Eiler J. (2021) Clumped isotope
777 effects of thermogenic methane formation: Insights from pyrolysis of hydrocarbons.
778 *Geochim. Cosmochim. Acta* **303**, 159-183.

779 Eiler J. M., Clog M., Lawson M., Lloyd M., Piasecki A., Ponton C., Xie H. (2017). The isotopic
780 structures of geological organic compounds. In *From Source to Seep: Geochemical*
781 *Applications in Hydrocarbon Systems*. (eds. M. Lawson, M. J. Formolo, and J. M. Eiler)
782 Geological Society, London, Special Publications, 468.

783 Ellis G. S., Dias R. F. (2022) Development of hydrocarbon gas reference materials for stable
784 isotopic composition ($\delta^{13}\text{C}$ and $\delta^2\text{H}$). U.S. Geological Survey Scientific Investigations report
785 2021-5136.

786 Erdmann M., Horsfield B. (2006) Enhanced late gas generation potential of petroleum source
787 rocks via recombination reactions: Evidence from the Norwegian North Sea. *Geochim.*
788 *Cosmochim. Acta* **70**, 3943-3956.

789 Gao L., Schimmelmann A., Tang Y. C., Mastalerz M. (2014) Isotope rollover in shale gas
790 observed in laboratory pyrolysis experiments: Insight to the role of water in thermogenesis
791 of mature gas. *Org. Geochem.* **68**, 95-106.

792 Gao L., He P. Q., Jin Y. B., Zhang Y. Q., Wang X. Q., Zhang S. C., Tang Y.C. (2016)
793 Determination of position-specific carbon isotope ratios in propane from hydrocarbon gas
794 mixtures. *Chem. Geol.* **435**, 1-9.

795 Giggenbach W. F. (1980) Geothermal gas equilibria. *Geochim. Cosmochim. Acta* **44**, 2021-2032.

796 Gilbert A., Yamada K., Suda K., Ueno Y., Yoshida N. (2016) Measurement of position-specific
797 ^{13}C isotopic composition of propane at the nanomole level. *Geochim. Cosmochim. Acta* **177**,
798 205-216.

799 Gilbert A., Lollar B. S., Musat F., Giunta T., Chen S. C., Kajimoto Y., Yamada K., Boreham C.
800 J., Yoshida N., Ueno Y. (2019) Intramolecular isotopic evidence for bacterial oxidation of
801 propane in subsurface natural gas reservoirs. *PNAS* **116**, 6653-6658.

802 Gilbert A. (2021) The organic isotopologue frontier. *Annu. Rev. Earth Planet. Sci.* **49**, 435-464.

803 He K., Zhang S. C., Mi J. K., Zhang W. L. (2018). The evolution of chemical groups and
804 isotopic fractionation at different maturation stages during lignite pyrolysis. *Fuel* **211**, 492-
805 506.

806 Horsfield B., Schenk H. J., Mills N., Welte D. H. (1992) An investigation of the in-reservoir
807 conversion of oil to gas: compositional and kinetic findings from closed-system programmed-
808 temperature pyrolysis. *Org. Geochem.* **19**, 191-204.

809 James A. T. (1983) Correlation of natural gas by use of carbon isotopic distribution between
810 hydrocarbon components. *AAPG Bull.* **67**, 1176-1191.

811 Jenden P. D., Drazan D. J., Kaplan I. R. (1993) Mixing of thermogenic natural gases in northern
812 Appalachian Basin. *AAPG Bull.* **77**. 980-998.

813 Jia W. L., Wang Q. L., Liu J. Z., Peng P. A., Liu B. H., Lu J. L. (2014). The effect of oil
814 expulsion or retention on further thermal degradation of kerogen at the high maturity stage:
815 A pyrolysis study of Type II kerogen from Pingliang shale, China. *Org. Geochem.* **71**, 17-
816 29.

817 Julien M., Goldman M. J., Liu C. J., Horita J., Boreham C. J., Yamada K., Green W. H., Yoshida
818 N., Gilbert A. (2020) Intramolecular ¹³C isotope distribution of butane from natural gas.
819 *Chem. Geol.* **541**, 119571.

820 Knauss K. G., Copenhaver S. A., Braun R. L., Burnham A. K. (1997) Hydrous pyrolysis of New
821 Albany and Phosphoria Shales: production kinetics of carboxylic acids and light
822 hydrocarbons and interactions between the inorganic and organic chemical systems. *Org.*
823 *Geochem.* **27**, 477-496.

824 Koyama T. (1963) Gaseous metabolism in lake sediments and paddy soils and the production of
825 atmospheric methane and hydrogen. *J. Geophys. Res.* **68**, 3971-3973.

826 Lewan M. D. (1983) Effects of thermal maturation on stable organic carbon isotopes as
827 determined by hydrous pyrolysis of Woodford Shale. *Geochim. Cosmochim. Acta* **47**, 1471-
828 1479.

829 Lewan M. D. (1997) Experiments on the role of water in petroleum formation. *Geochim.*
830 *Cosmochim. Acta* **61**, 3691-3723.

- 831 Lewan M. D. (1998) Sulphur-radical control on petroleum formation rates. *Nature* **391**, 164-166.
- 832 Lewan M. D., Kotarba M. J., Wieclaw D., Piestrzyński A. (2008). Evaluating transition-metal
833 catalysis in gas generation from the Permian Kupferschiefer by hydrous pyrolysis. *Geochim.*
834 *Cosmochim. Acta* **72**, 4069-4093.
- 835 Lewan M. D., Kotarba M. J. (2014) Thermal-maturity limit for primary thermogenic-gas
836 generation from humic coals as determined by hydrous pyrolysis. *AAPG Bull.* **98**, 2581-2610.
- 837 Liu C. J., McGovern G. P., Liu P., Zhao H., Horita J. (2018) Position-specific carbon and
838 hydrogen isotopic compositions of propane from natural gases with quantitative NMR.
839 *Chem. Geol.* **491**, 14-26.
- 840 Liu C. J., Liu P., McGovern G. P., Horita J. (2019) Molecular and intramolecular isotope
841 geochemistry of natural gases from the Woodford Shale, Arkoma Basin, Oklahoma.
842 *Geochim. Cosmochim. Acta* **255**, 188-204.
- 843 Liu Q. Y., Jin Z. J., Meng Q. Q., Wu X. Q., Jia H. C. (2015) Genetic types of natural gas and
844 filling patterns in Daniudi gas field, Ordos Basin, China. *J. Asian Earth Sci.* **107**, 1-11.
- 845 Li X. Q., Krooss B. M., Weniger P., Littke R. (2015) Liberation of molecular hydrogen (H₂) and
846 methane (CH₄) during non-isothermal pyrolysis of shales and coals: Systematics and
847 quantification. *Int. J. Coal Geol.* **137**, 152-164.
- 848 Li X. Q., Krooss B. M., Weniger P., Littke R. (2017) Molecular hydrogen (H₂) and light
849 hydrocarbon gases generation from marine and lacustrine source rocks during closed-system
850 laboratory pyrolysis experiments. *J. Anal. Appl. Pyrolysis* **126**, 275-287.
- 851 Li X. Q., McGovern G. P., Horita J. (2021) Kinetics of propane cracking and position-specific
852 isotope fractionation: Insights into the origins of natural gases. *Org. Geochem.* **155**, 104234.
- 853 Li Y., Zhang L., Xiong Y. Q., Gao S. T., Yu Z. Q., Peng P. A. (2018) Determination of position-
854 specific carbon isotope ratios of propane from natural gas. *Org. Geochem.* **119**, 11-21.
- 855 Lorant F., Prinzhofer A., Behar F., Huc A. Y. (1998) Carbon isotopic and molecular constraints
856 on the formation and the expulsion of thermogenic hydrocarbon gases. *Chem. Geol.* **147**,
857 249-264.

858 Lorant F., Behar F. (2002) Late generation of methane from mature kerogens. *Energy Fuels* **16**,
859 412-427.

860 Ma X. X., Zheng J. J., Zheng G. D., Xu W., Qian Y., Xia Y. Q., Wang Z. D., Wang X. F., Ye X.
861 Y. (2016) Influence of pyrite on hydrocarbon generation during pyrolysis of type-III
862 kerogen. *Fuel* **167**, 329-336.

863 Machel H. G. (2001). Bacterial and thermochemical sulfate reduction in diagenetic settings – old
864 and new insights. *Sediment. Geol.* **140**, 143-175.

865 Mahlstedt N., Horsfield B. (2012) Metagenetic methane generation in gas shales I. Screening
866 protocols using immature samples. *Mar. Pet. Geol.* **31**, 27-42.

867 Mango F. D. (1992) Transition metal catalysis in the generation of petroleum and natural gas.
868 *Geochim. Cosmochim. Acta* **56**, 553-555.

869 Mango F. D., Jarvie D., Herriman E. (2009) Natural gas at the thermodynamic equilibrium.
870 Implications for the origin of natural gas. *Geochem. Trans.* **10**, 6.

871 Michels R., Enjelvin-Raoult N., Elie M., Mansuy L., Faure P., Oudin J-L. (2002) Understanding
872 of reservoir gas compositions in a natural case using stepwise semi-open artificial maturation.
873 *Mar. Pet. Geol.* **19**, 589-599.

874 Morita R. Y. (1999). Is H₂ the universal energy source for long-term survival? *Microb. Ecol.* **38**,
875 307-320.

876 Newell K. D., Doveton J. H., Merriam D. F., Lollar B. S., Waggoner W. M., Magsuson L. M. (2007)
877 H₂-rich and hydrocarbon gas recovered in a deep Precambrian well in Northeastern Kansas.
878 *Nat. Resour. Res.* **16**, 277-292.

879 Ni Y. Y., Ma Q. S., Ellis G. S., Dai J. X., Katz B., Zhang S. C., Tang Y. C. (2011) Fundamental
880 studies on kinetics isotope effect (KIE) of hydrogen isotope fractionation in natural gas
881 systems. *Geochim. Cosmochim. Acta* **75**, 2696-2707.

882 Ni Y. Y., Gao J. L., Chen J. P., Liao F. R., Liu J. Q., Zhang D. J. (2018) Gas generation and its
883 isotope composition during coal pyrolysis: Potential mechanism of isotope rollover. *Fuel*
884 **231**, 387-395.

- 885 Orr W. L. (1977) Geologic and geochemical controls on the distribution of hydrogen sulfide in
886 natural gas. In *Advances in Organic Geochemistry 1975* (eds. Campos, R. and Goni, J.).
887 Pergamon Press, Oxford, pp. 571-597.
- 888 Pepper A. S., Corvit P. J. (1995) Simple kinetic models of petroleum formation. Part I: oil and
889 gas generation from kerogen. *Mar. Pet. Geol.* **12**, 291-319.
- 890 Pepper A. S., Dodd T. A. (1995) Simple kinetic models of petroleum formation. Part II: oil-gas
891 cracking. *Mar. Pet. Geol.* **12**, 321-340.
- 892 Peterson B. K., Formolo M. J., Lawson M. (2018) Molecular and detailed isotopic structures of
893 petroleum: Kinetic Monte Carlo analysis of alkane cracking. *Geochim. Cosmochim. Acta*
894 **243**, 169-185.
- 895 Piasecki A., Sessions A., Lawson M., Ferreira A. A., Neto Santos E. V., Eiler J. M. (2016)
896 Analysis of the site-specific carbon isotope composition of propane by gas source isotope
897 ratio mass spectrometer. *Geochim. Cosmochim. Acta* **188**, 58-72.
- 898 Piasecki A., Sessions A., Lawson M., Ferreira A. A., Neto Santos E.V., Ellis G. S., Lewan M.
899 D., Eiler J. M. (2018) Position-specific ¹³C distributions within propane from experiments
900 and natural gas samples. *Geochim. Cosmochim. Acta* **220**, 110-124.
- 901 Polyakov V. B., Horita J. (2021) Equilibrium carbon isotope fractionation factors of hydrocarbons:
902 Semi-empirical force-field method. *Chem. Geol.* **559**, 119948.
- 903 Price L. C., Schoell M. (1995) Constraints on the origins of hydrocarbon gas from the
904 compositions of gases at their site of origin. *Nature* **378**, 268-371.
- 905 Reeves E. P., Seewald J. S., Sylva S. P. (2012) Hydrogen isotope exchange between n-alkanes
906 and water under hydrothermal conditions. *Geochim. Cosmochim. Acta* **77**, 582-599.
- 907 Rodriguez N. D., Philp R. P. (2010) Geochemical characterization of gases from Mississippian
908 Barnett Shale, Fort Worth Basin, Texas. *AAPG Bull.* **94**, 1641-1656.
- 909 Sanna A., Uibu M., Caramanna G., Kuusik R., Maroto-Valer M. M. (2014) A review of mineral
910 carbonation technologies to sequester CO₂. *Chem. Soc. Rev.* **43**, 8049-8080.

- 911 Schimmelmann A., Lewan M. D., Wintsch R. P. (1999) D/H isotope ratios of kerogen, bitumen,
912 oil, and water in hydrous pyrolysis of source rocks containing kerogen type I, II, IIS and III.
913 *Geochim. Cosmochim. Acta* **63**, 3751-3766.
- 914 Schoell M. (1988) Multiple origins of methane in the earth. *Chem. Geol.* **71**, 1-10.
- 915 Sessions A. L., Sylva S. P., Summons R. E., Hayes J. M. (2004). Isotopic exchange of carbon-
916 bound hydrogen over geological timescales. *Geochim. Cosmochim. Acta* **68**, 1545-1559.
- 917 Seewald J. S. (2001) Aqueous geochemistry of low molecular weight hydrocarbons at elevated
918 temperatures and pressures: Constraints from minerals buffered laboratory experiments.
919 *Geochim. Cosmochim. Acta* **65**, 1641-1644.
- 920 Shao D. Y., Zhang T. W., Ko L. T., Li Y. F., Yan J. P., Zhang L. L., Luo H., Qiao B. (2020)
921 Experimental investigation of oil generation, retention, and expulsion within Type II
922 kerogen-dominated marine shales: Insights from gold-tube nonhydrous pyrolysis of Barnett
923 and Woodford Shales using miniature core plugs. *Int. J. Coal Geol.* **217**, 103337.
- 924 Snowdon L. R. (2001) Natural gas composition in a geological environment and the implications
925 of the process of generation and preservation. *Org. Geochem.* **32**, 913-931.
- 926 Shuai Y. H., Douglas P. M. J., Zhang S. C., Stolper D. A., Ellis G. S., Lawson M., Lewan M. D.,
927 Formolo M., Mi J. K., He K., Hu G. Y., Eiler J. M. (2018) Equilibrium and non-equilibrium
928 controls on the abundances of clumped isotopologues of methane during thermogenic
929 formation in laboratory experiments: Implications for the chemistry of pyrolysis and the
930 origins of natural gases. *Geochim. Cosmochim. Acta* **223**, 159-174.
- 931 Suda K., Gilbert A., Yamada K., Yoshida N., Ueno Y. (2017) Compound- and position-specific
932 carbon isotopic signatures of abiogenic hydrocarbons from on-land serpentinite-hosted
933 Hakuba Happo hot spring in Japan. *Geochim. Cosmochim. Acta* **206**, 201-215.
- 934 Sugisaki R., Nagamine K. (1995) Evolution of light hydrocarbon gases in subsurface processes:
935 Constraints from chemical equilibrium. *Earth Planet. Sci. Lett.* **133**, 151-161.
- 936 Sweeney J. J., Burnham A. K. (1990) Evaluation of a simple model of vitrinite reflectance based
937 on chemical kinetics. *AAPG Bull.* **74**, 1559-1570.
- 938 Tang Y., Perry J. K., Jende P. D., Schoell M. (2000) Mathematical modeling of stable carbon
939 isotope ratios in natural gases. *Geochim. Cosmochim. Acta* **64**, 2673-2687.

- 940 Tassi F., Vaselli O., Capaccioni B., Montegrossi G., Barahona F., Caprai A. (2007) Scrubbing
941 process and chemical equilibria controlling the composition of light hydrocarbons in natural
942 gas discharges: An example from the geothermal fields of EI Salvador. *Geochem. Geophys.*
943 *Geosystems* **8**, 5.
- 944 Thiagarajan N., Xie H., Ponton C., Kitchen N., Peterson B., Lawson M., Formolo M., Xiao Y.
945 T., Eiler J. (2020) Isotopic evidence for quasi-equilibrium chemistry in thermally mature
946 natural gases. *PNAS* **117**, 3989-3995.
- 947 Tian H., Xiao X. M., Wilkins R. W. T., Tang Y. C. (2012) An experimental comparison of gas
948 generation from three oil fractions: Implications for the chemical and stable carbon isotopic
949 signatures of oil cracking gas. *Org. Geochem.* **46**, 96-112.
- 950 Tian H., Xiao X. M., Wilkins R. W. T., Tang, Y. C. (2008) New insights into the volume and
951 pressure changes during the thermal cracking of oil to gas in reservoirs: Implications for the
952 in-situ accumulation of gas cracked from oils. *AAPG Bull.* **92**, 181-200.
- 953 Tingay M. R. P., Morley C. K., Laird A. L., Limpornpipat O., Krisadasima K., Pabchanda S.,
954 Macintyre H. R. (2013) Evidence for overpressure generation by kerogen to gas maturation
955 in the northern Malay Basin. *AAPG Bull.* **97**, 639-672.
- 956 Turner A. C., Korol R., Eldridge D. L., Bill M., Conrad M. E., Miller III T. F., Stolper D. A. (2021)
957 Experimental and theoretical determinations of hydrogen isotopic equilibrium in the system
958 CH₄-H₂-H₂O from 3 to 200 °C. *Geochim. Cosmochim. Acta* **314**, 223-269.
- 959 Wang D. T., Reeves E. P., McDermott J. M., Seewald J. S., Ono S. (2018) Clumped
960 isotopologue constraints on the origin of methane at seafloor hot springs. *Geochim.*
961 *Cosmochim. Acta* **223**, 141-158.
- 962 Webb M. A., Miller T. F. (2014). Position-specific and clumped stable isotope studies:
963 Comparison of the Urey and path-integral approaches for carbon dioxide, nitrous oxide,
964 methane, and propane. *J. Phys. Chem. A* **118**, 467-474.
- 965 Wei L., Schimmelmann A., Mastalerz M., Lahann R. W., Sauer P. E., Drobniak A., Strapoć D.,
966 Mango F. D. (2018) Catalytic generation of methane at 60 - 100 °C and 0.1 - 300 MPa from

967 source rocks containing kerogen Types I, II and III. *Geochim. Cosmochim. Acta* **231**, 88-
968 116.

969 Whiticar M. J. (1999) Carbon and hydrogen isotope systematic of microbial formation and
970 oxidation of methane. *Chem. Geol.* **161**, 291-314.

971 Worden R. H., Smalley P. C., Oxtoby N. H. (1995) Gas souring by thermochemical sulfate
972 reduction at 140 °C. *AAPG Bull.* **79**, 854-863.

973 Xia X. Y. (2014) Kinetics of gaseous hydrocarbon generation with constraints of natural gas
974 composition from Barnett Shale. *Org. Geochem.* **74**, 143-149.

975 Xie H., Ponton C., Formolo M. J., Lawson M., Peterson B. K., Lloyd M. K., Sessions A. L., Eiler
976 J. M. (2018) Position-specific hydrogen isotope equilibrium in propane. *Geochim.*
977 *Cosmochim. Acta* **238**, 193-207.

978 Xie H., Ponton C., Formolo M. J., Lawson M., Ellis G. S., Lewan M. D., Ferreira A. A., Morais
979 E. T., Spigolon A. L. D., Sessions A. L., Eiler J. M. (2020) Position-specific distribution of
980 hydrogens in natural propane: Effects of thermal cracking, equilibration and biodegradation.
981 *Geochim. Cosmochim. Acta* **290**, 235-256.

982 Xie H., Formolo M., Eiler J. (2022) Predicting isotopologue abundances in the products of
983 organic catagenesis with a kinetic Monte-Carlo model. *Geochim. Cosmochim. Acta* **327**,
984 200-228.

985 Zgonnik V. (2020) The occurrence and geoscience of natural hydrogen: A comprehensive
986 review. *Earth Sci. Rev.* **203**, 103140.

987 Zhang L., Li Y., Jiang W. M., Xiong Y. Q. (2022) Position-specific carbon isotopic composition
988 of thermogenic propane: Insights from pyrolysis experiments. *Org. Geochem.* **166**, 104379.

989 Zhao H., Liu C. J., Larson T. E., McGovern G. P., Horita J. (2020) Bulk and position-specific
990 isotope geochemistry of natural gases from the Late Cretaceous Eagle Ford Shale, south
991 Texas. *Mar. Pet. Geol.* **122**, 104659.

992 Zumberge J., Ferworn K., Brown S. (2012) Isotopic reversal ('rollover') in shale gases produced
993 from the Mississippian Barnett and Fayetteville formations. *Mar. Pet. Geol.* **31**, 43-52.

Fig. 1. Molar yields of C₁-C₅ gases in the pyrolysis of Woodford Shale as a function of thermal maturity (Easy %R_o), compared with the pyrolysis data of the Woodford kerogen (Lewan, 1997). The yields of C₄ and C₅ include both normal and iso alkanes. The kinetic model for kerogen cracking (Knauss et al., 1997; Xia, 2014), oil cracking (Tian et al., 2008), propane cracking (Tian et al., 2008; Li et al., 2021) are also shown.

Fig. 2. Evolution of total hydrocarbon gas yields (C₁-C₅) and molar ratios (C₁/(C₁-C₅)) with maturities, compared with the previous studies on the pyrolysis of Woodford Shale (Lewan, 1997; Shuai et al., 2018) and natural Woodford Shale gas (Liu et al., 2019). The kinetic calculations of C₁-C₅ yields at kerogen cracking (Pepper and Corvit, 1995) and oil cracking stages (Pepper and Dodd, 1995), as well as C₁-C₃ yields based on Knauss et al. (1997) are shown. The predicted gas dryness (Knauss et al., 1997) at a heating rate of 10 °C/m.y. is indicated.

Fig. 3. C and H isotope compositions of CH₄, C₂H₆ and C₃H₈ in the pyrolysis gases from Woodford Shale, with the comparison of natural Woodford Shale gas (Liu et al., 2019) and another hydrous pyrolysis study of the Woodford kerogen (Shuai et al., 2018).

Fig. 4. (a) Position-specific carbon isotope deviations of propane ($\Delta C_{c-t} = \delta^{13}C_{center} - \delta^{13}C_{terminal}$) in the pyrolysis of Woodford Shale with the comparison of natural Woodford Shale gas (Liu et al., 2019), Eagle Ford Shale gas (Zhao et al., 2020). It also includes another hydrous pyrolysis of Woodford kerogen (Piasecki et al., 2018), n-C₂₅ cracking (Gilbert et al., 2019), C₃H₈ cracking (Li et al., 2021), and the equilibrium model (color bar) (Webb and Miller, 2014). The original data from Woodford kerogen cracking (Piasecki et al., 2018) is normalized in Gilbert et al. (2019). (b) $\delta^{13}C_{ter}$ and $\delta^{13}C_{cen}$ in this study compared with Woodford Shale gas (Liu et al., 2019). The predicted position-specific $\delta^{13}C$ values of propane at 150 and 310 °C were calculated based on Tang et al. (2000)

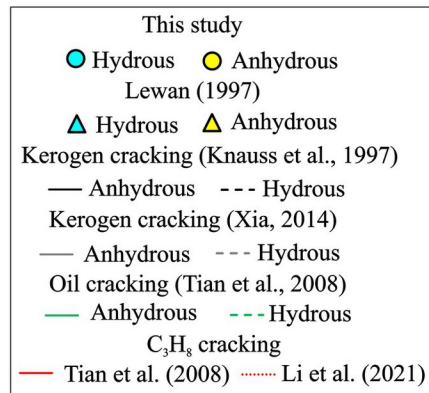
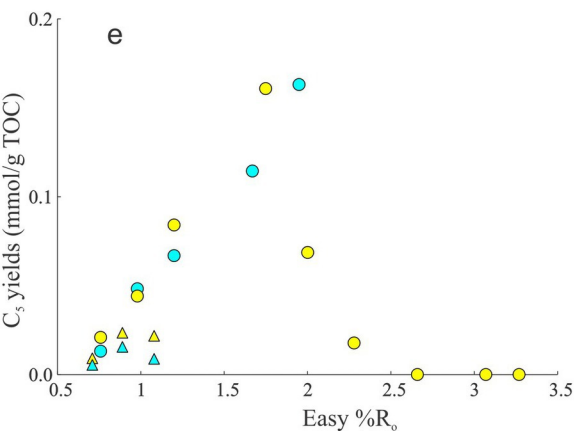
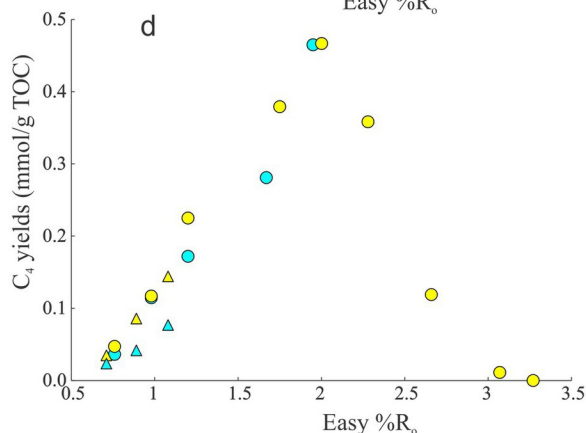
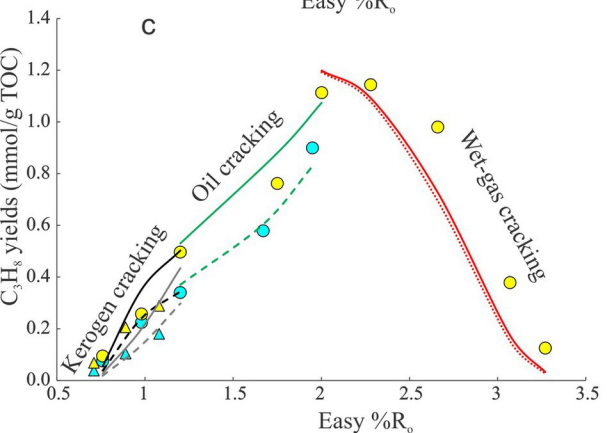
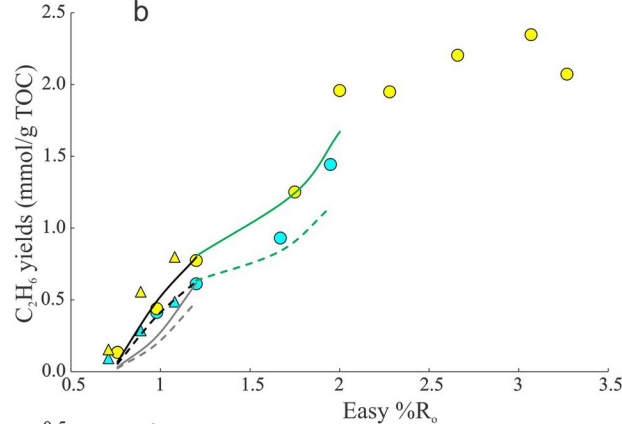
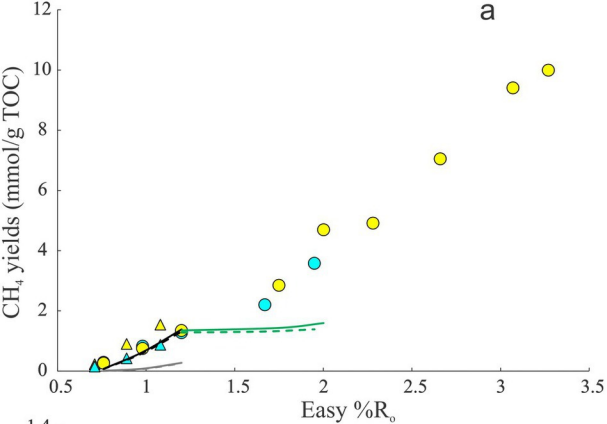
Fig. 5. Arrhenius plot of the rate constants determined from the anhydrous pyrolysis of Woodford Shale at 310 to 480 °C, compared with C₁-C₃ gas generation from the cracking of marine New Albany Shale (Knauss et al., 1997), Barnett Shale (Xia, 2014), oil (Tian et al., 2008). Propane cracking from the other studies (Tian et al., 2008; Li et al., 2021) are also shown.

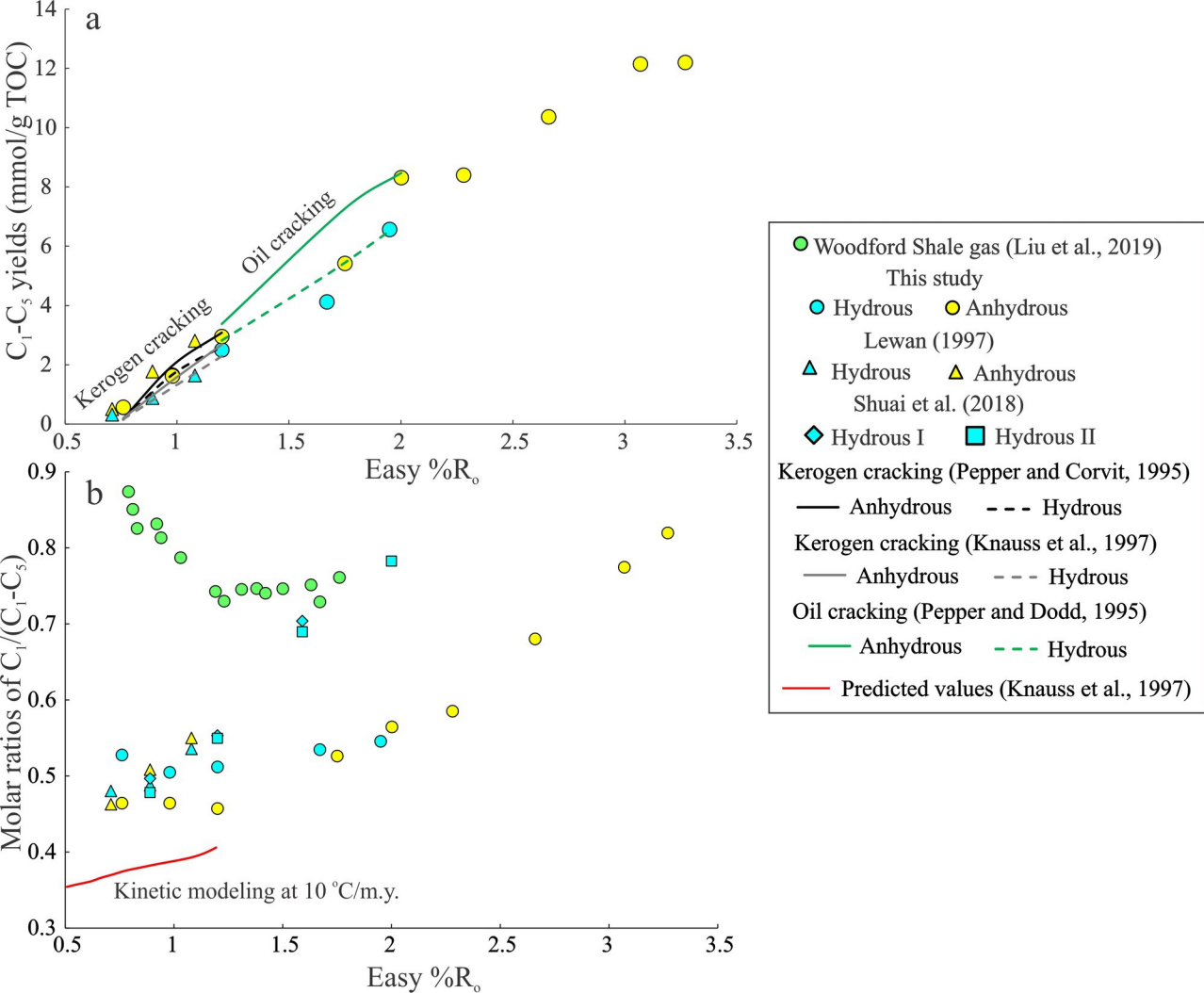
Fig. 6. Thermodynamic data of gaseous species in the natural Woodford Shale reservoir (Liu et al., 2019) and pyrolysis conditions, including the theoretical calculation on the equilibrium constants (Barin, 1995; Tassi et al., 2007) and pressure effect (Danesh, 1998).

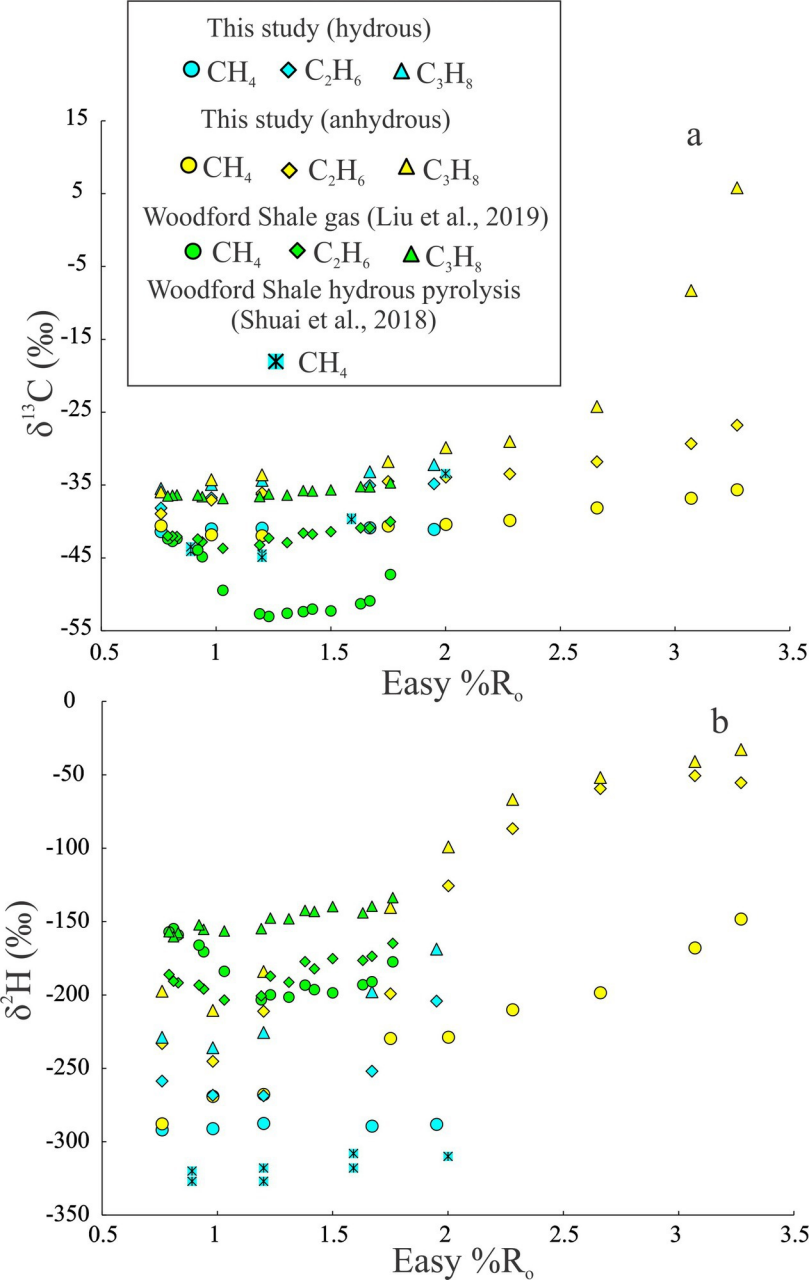
Fig. 7. δ^2H of C₁-C₃ in the natural (Liu et al., 2019) and pyrolysis gas (this study, Shuai et al., 2018) from the Woodford kerogen, compared with three δ^2H modelling for capping H: kinetic abstraction from hydrocarbons (H KIE), capping H equilibrated with water (H exchange), and full H exchange with water (Full exchange). The data of equilibrium isotope effect from the previous studies (Thiagarajan et al., 2020; Turner et al., 2021).

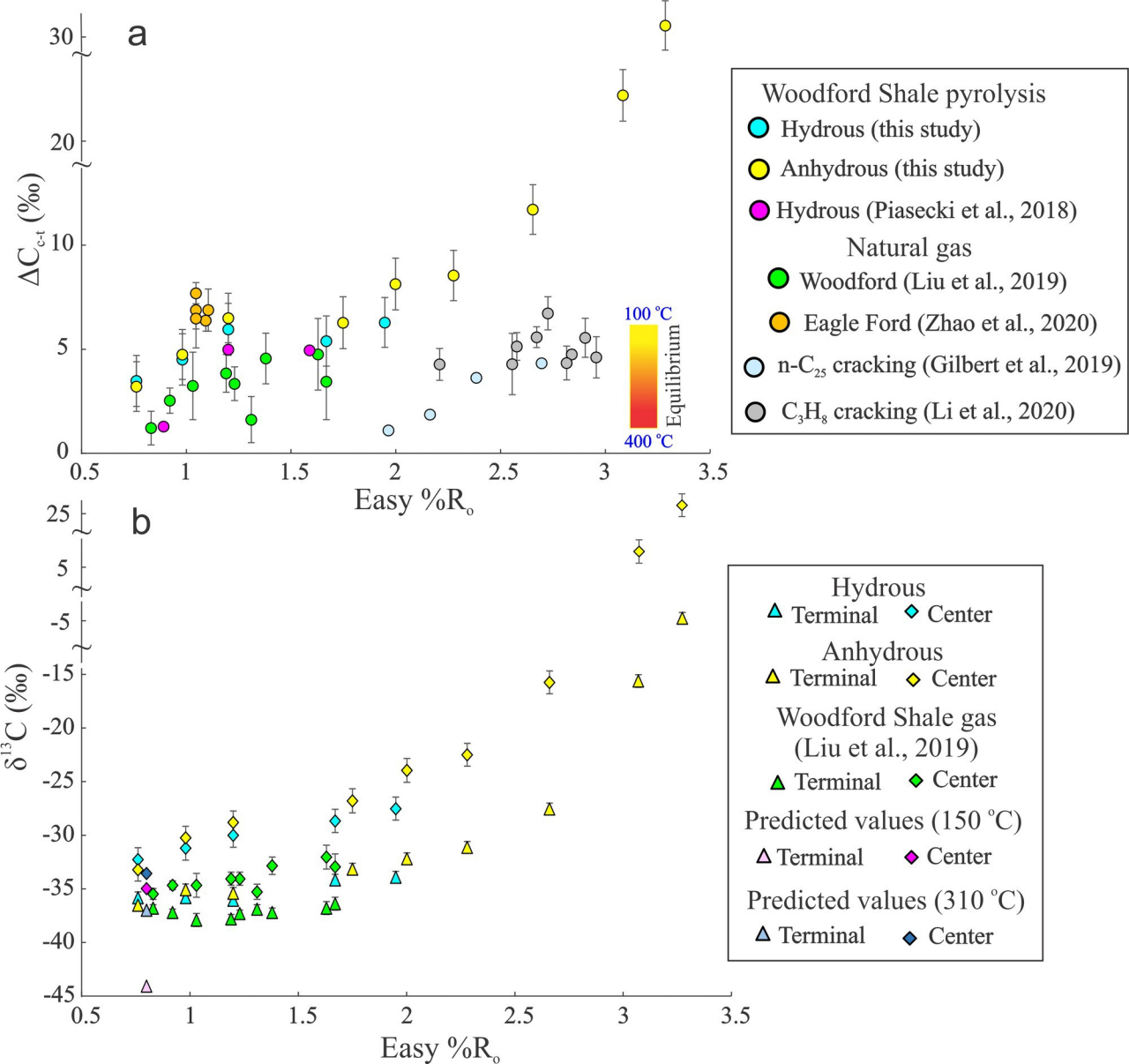
Fig. 8. $\delta^{13}C$ (a, b) and δ^2H (c, d) isotope equilibria among C₁-n-C₄ gases in natural (Liu et al., 2019) Woodford Shale gas and pyrolysis gas, compared with the theoretical equilibrium values (Thiagarajan et al., 2020; Polyakov and Horita, 2021) and kinetic calculation (Ni et al., 2011).

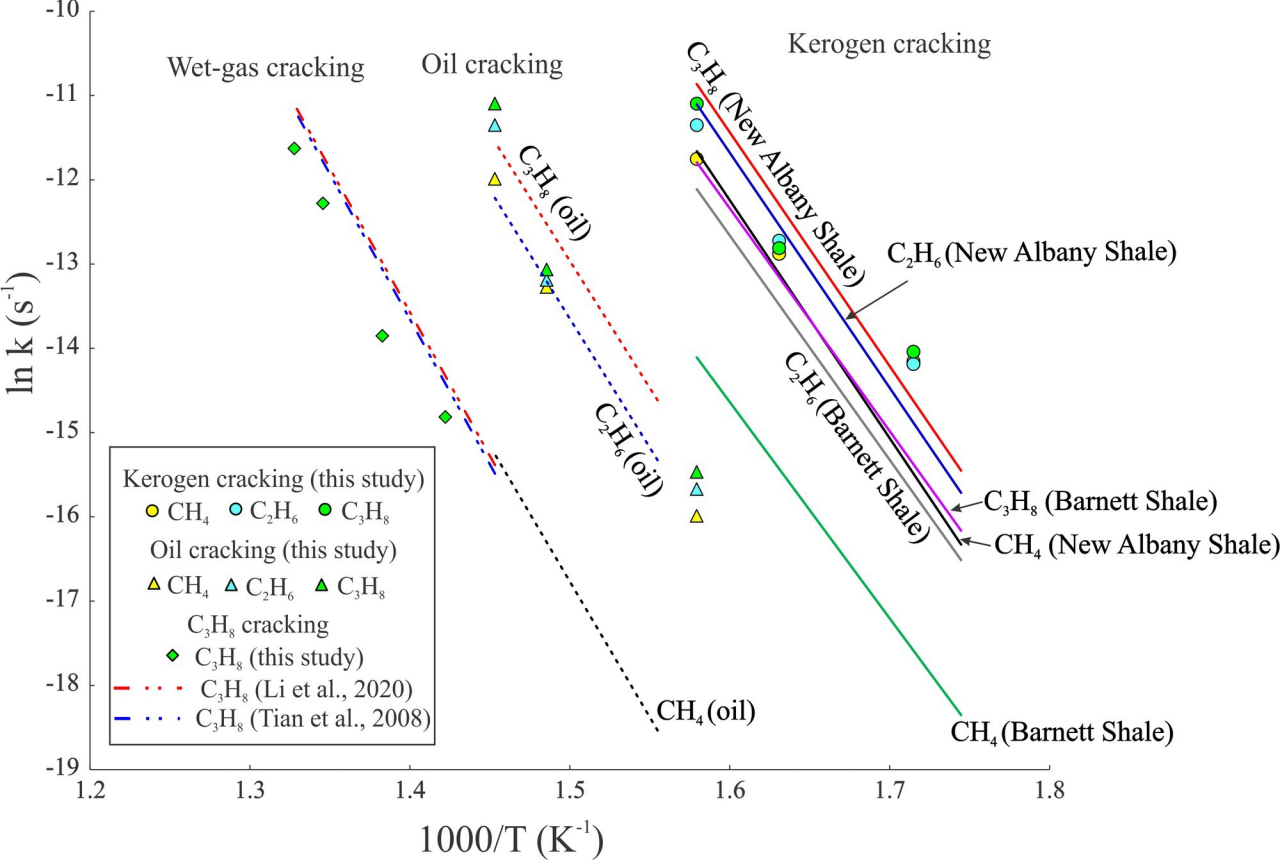
Fig. 9. Summary of position-specific C (a) and H (b) of propane from this study, literature data of natural gas samples (Suda et al., 2017; Liu et al., 2018, 2019; Piasecki et al., 2018; Gilbert et al., 2019; Xie et al., 2020; Zhao et al., 2020; Zhang et al., 2022), compared with propane generation from theoretical modeling on the cracking of n-C₄₀/n-C₂₀ (Peterson et al., 2018) and type I kerogen (Xie et al., 2022). C₃H₈ cracking (Li et al., 2021), biodegradation (Gilbert et al., 2019) and diffusion (Piasecki et al., 2016) are also indicated. The thermal maturities (%R_o) and temperature (°C) of gas samples (b) are marked and the arrow indicates the increase of maturity in Woodford Shale gas. Position-specific $\delta^{13}C$ and δ^2H values of propane at equilibrium state at 50, 100 and 200 °C are calculated according to Webb and Miller (2014).

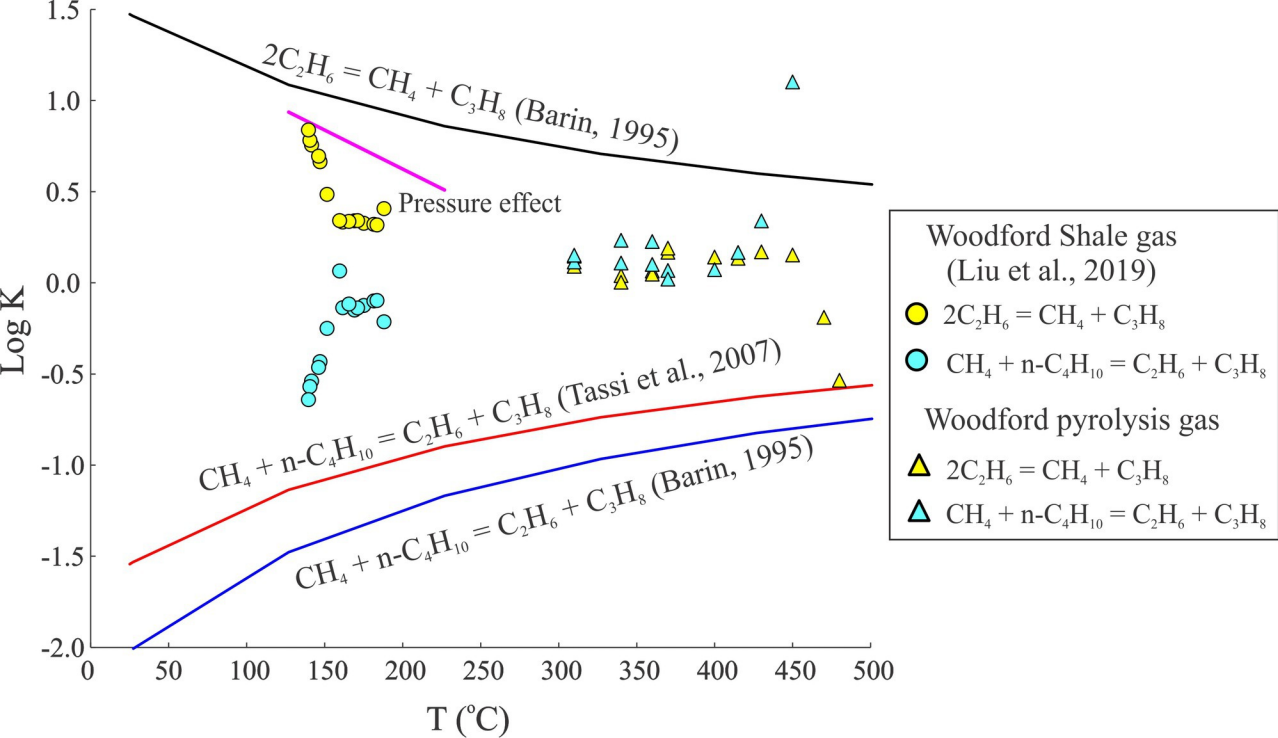


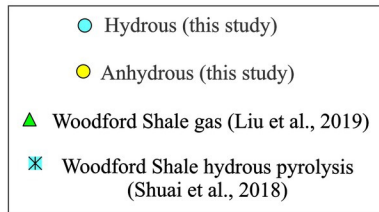
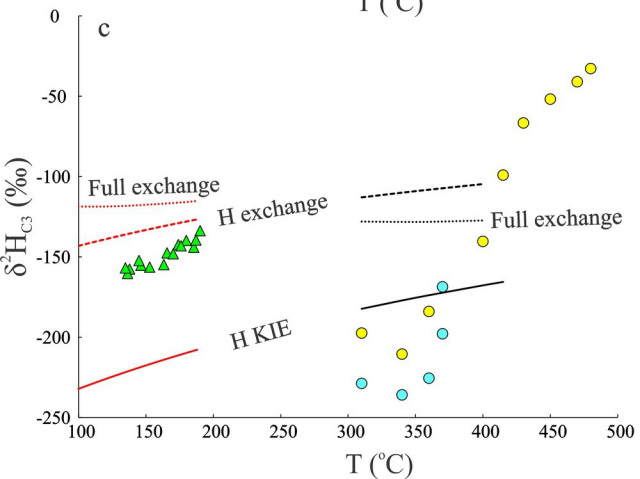
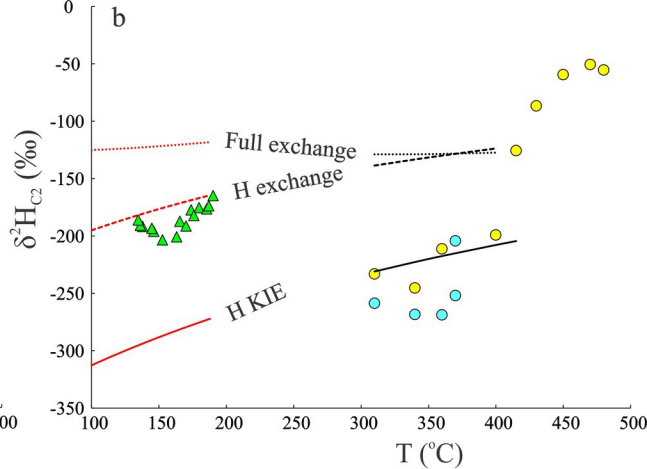
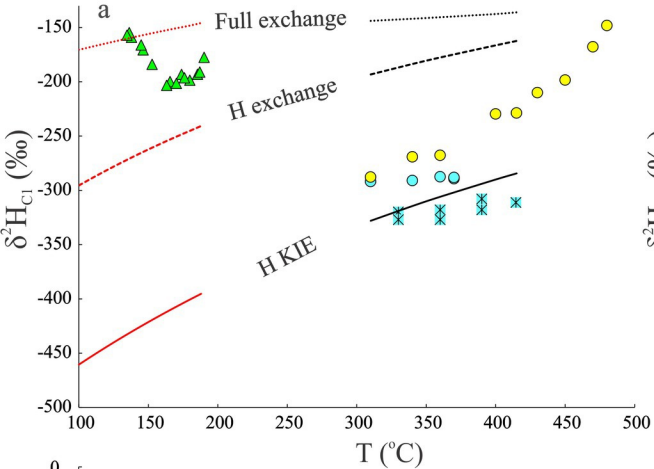


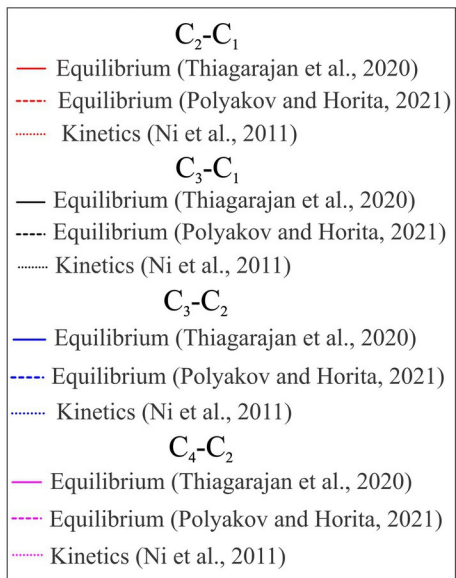
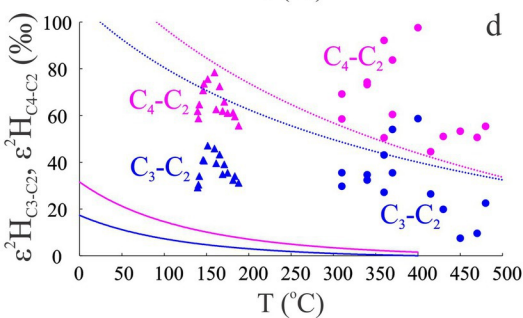
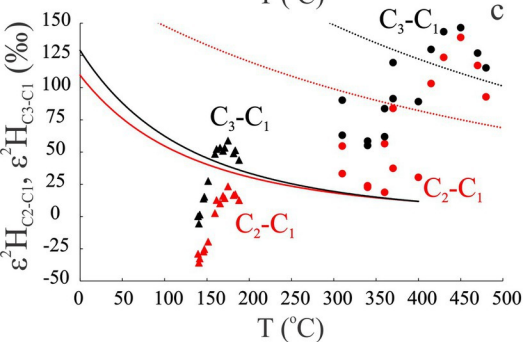
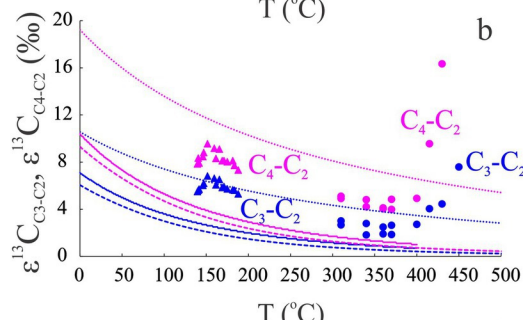
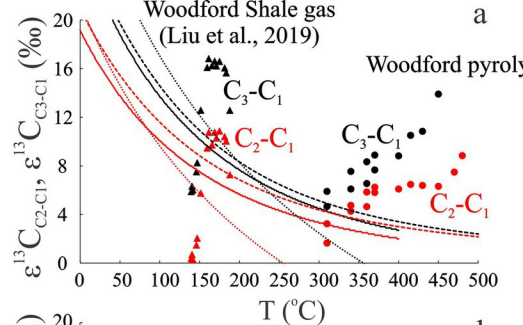


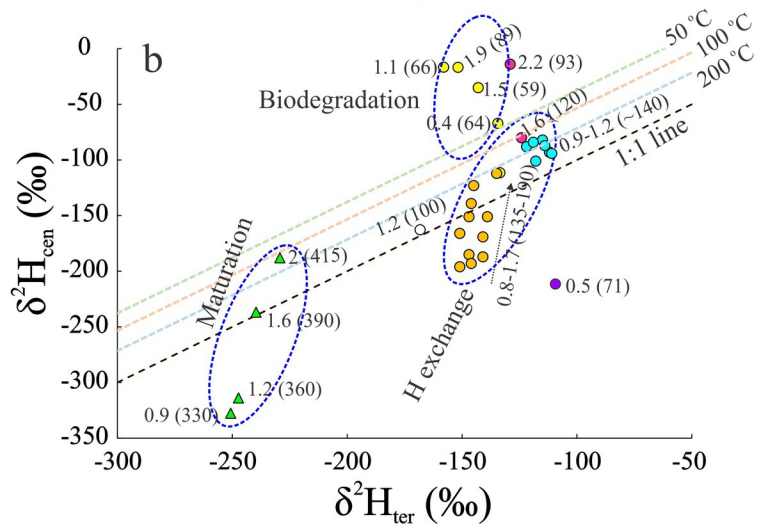
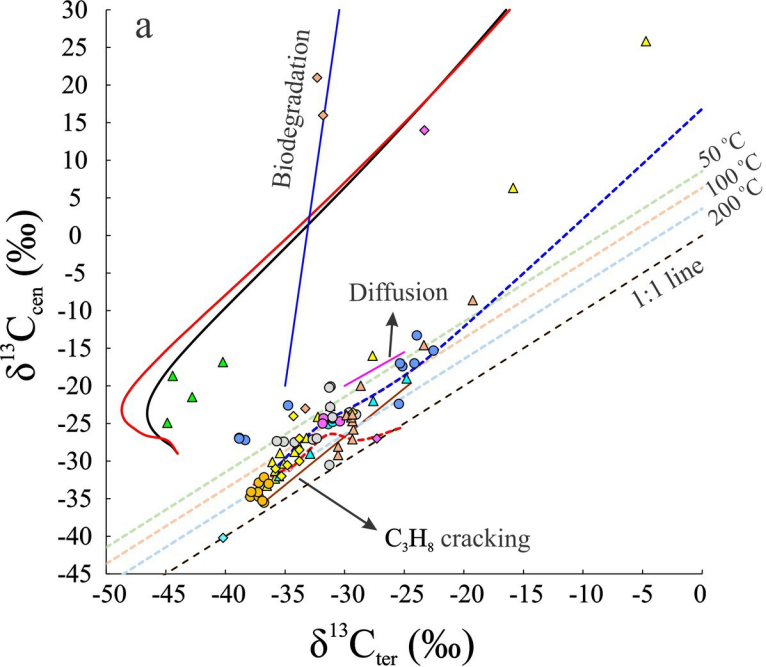












Natural gas

- Woodford (Liu et al., 2019)
- Eagle Ford (Zhao et al., 2020)
- Eagle Ford (Piasecki et al., 2018)
- Potiguar (Piasecki et al., 2018)
- Potiguar (Xie et al., 2020)
- Hogsback (Xie et al., 2020)
- Briggs (Xie et al., 2020)
- Gulf of Mexico (Xie et al., 2020)
- Tarim (Zhang et al., 2022)
- ◆ Carnarvon (Gilbert et al., 2019)
- ◆ Michigan (Gilbert et al., 2019)
- ◆ Southwest Ontario (Gilbert et al., 2019)
- ◆ Hakuba Happo hot spring (Suda et al., 2017)

Pyrolysis gas

- ▲ Woodford (this study)
- ▲ Woodford (Piasecki et al., 2018; Xie et al., 2020)
- ▲ n- C_{25} (Gilbert et al., 2019)
- ▲ Type II kerogen (Zhang et al., 2022)

kMC modelling

- n- C_{20} cracking (Peterson et al., 2018)
- n- C_{40} cracking (Peterson et al., 2018)
- - - Type I kerogen scheme A (Xie et al., 2022)
- - - Type I kerogen scheme B (Xie et al., 2022)

Table 1. Experimental conditions and measured yields of gaseous species produced from the pyrolysis of Woodford Shale in the closed system with and without added DI water.

Table 2. Isotope compositions of HC gases, H₂ and H₂S from the pyrolysis of the Woodford Shale.

Table 3. Position-specific C isotopic compositions of propane in the pyrolysis gas from the Woodford Shale. $\delta^{13}\text{C}_{\text{ter}}$: carbon isotope in terminal position; $\delta^{13}\text{C}_{\text{cen}}$: carbon isotope at central position; $\Delta\text{C}_{\text{c-t}}$: position-specific carbon isotope deviation ($\delta^{13}\text{C}_{\text{cen}} - \delta^{13}\text{C}_{\text{ter}}$); std: standard deviation.

Type	T (°C)	Easy %R _o	HC gas yield (C ₁ -C ₅) (mmol/g TOC)	Gas yield (mmol/g TOC)									C ₁ /(C ₁ -C ₅)
				CH ₄	C ₂ H ₆	C ₃ H ₈	C ₃ H ₆	C ₄	C ₅	H ₂	CO ₂	H ₂ S	
Hy	310	0.76	0.6	0.29	0.13	0.08	0.00	0.04	0.01	0.05	1.17	0.71	0.53
	340	0.98	1.6	0.83	0.41	0.22	0.01	0.11	0.05	0.47	1.89	1.26	0.50
	360	1.2	2.5	1.28	0.61	0.34	0.03	0.17	0.07	0.63	1.86	1.59	0.51
	370	1.67	4.1	2.20	0.93	0.58	0.01	0.28	0.11	0.46	1.90	2.85	0.53
	370	1.95	6.6	3.58	1.44	0.90	0.01	0.46	0.16	0.49	2.14	2.33	0.55
Anhy	310	0.76	0.6	0.26	0.13	0.09	0.01	0.05	0.02	0.06	0.82	0.54	0.46
	340	0.98	1.6	0.75	0.44	0.26	0.01	0.12	0.04	0.32	1.00	0.72	0.46
	360	1.2	2.9	1.35	0.77	0.50	0.02	0.22	0.08	0.71	1.04	1.09	0.46
	400	1.75	5.4	2.85	1.25	0.76	0.01	0.38	0.16	0.69	1.11	2.06	0.53
	415	2.00	8.3	4.69	1.96	1.11	0.01	0.47	0.07	0.59	1.19	1.97	0.56
	430	2.28	8.4	4.91	1.95	1.14	0.01	0.36	0.02	0.66	0.50	3.33	0.59
	450	2.66	10.4	7.05	2.20	0.98	0.01	0.12	0.00	0.86	0.92	2.88	0.68
	470	3.07	12.1	9.41	2.35	0.38	0.00	0.01	0.00	0.99	0.93	2.21	0.77
	480	3.27	12.2	9.99	2.07	0.13	0.00	0.00	0.00	1.09	1.03	2.11	0.82

Easy %R_o is calculated based on temperature and time program in the pyrolysis experiments according to Sweeney and Burnham (1990).

Hy: hydrous experiments; Anhy: anhydrous experiments.

CO₂ and H₂S yields in hydrous conditions include those in gaseous phase (measured) and aqueous phase (calculated).

Type	T (°C)	Easy %R _o	δ ¹³ C (‰)							δ ² H (‰)									
			CH ₄	C ₂ H ₆	C ₃ H ₈	i-C ₄	n-C ₄	i-C ₅	n-C ₅	CO ₂	CH ₄	C ₂ H ₆	C ₃ H ₈	i-C ₄	n-C ₄	i-C ₅	n-C ₅	H ₂	H ₂ S
Hy	310	0.76	-41.4	-38.1	-35.5	-32.6	-33.2	-30.5	-31.0	-31.0	-292	-259	-229	-209	-189	-196	-155	-393	-543
	340	0.98	-41.0	-36.7	-34.9	-31.7	-32.5	-30.5	-30.3	-30.2	-291	-268	-236	-219	-195	-201	-157	-380	-543
	360	1.2	-40.9	-36.3	-34.4	-31.9	-32.2	-30.0	-29.8	-29.9	-288	-269	-226	-192	-177	-196	-152	-376	-538
	370	1.67	-40.8	-35.0	-33.2	-30.8	-31.1	-28.7	-29.1	-29.3	-289	-252	-198	-175	-168	-172	-138	-362	-537
	370	1.95	-41.1	-34.8	-32.2	-30.3	-30.0	-27.8	-27.4	-29.4	-288	-204	-169	-146	-144	-119	-141	-383	-537
Anhy	310	0.76	-40.6	-38.9	-35.9	-33.5	-33.8	-31.3	-31.6	-31.2	-288	-233	-198	-171	-175	-147	-170	-461	-536
	340	0.98	-41.8	-37.1	-34.3	-31.8	-32.2	-29.6	-30.0	-30.5	-269	-245	-211	-179	-171	-176	-136	-373	-541
	360	1.2	-41.9	-36.1	-33.6	-31.6	-32.0	-30.2	-30.0	-30.0	-268	-211	-184	-139	-161	-117	-149	-368	-540
	400	1.75	-40.6	-34.5	-31.8	-30.3	-29.6	-26.4	-26.5	-29.5	-230	-199	-140	-113	-102	-115	-69	-283	-543
	415	2.00	-40.4	-33.9	-29.9	-28.3	-24.3	-16.6	-14.9	-28.8	-229	-126	-99	-96	-81	-47	-68	-324	-542
	430	2.28	-39.9	-33.5	-29.0	-26.8	-17.1	-6.6	0.1	-26.9	-210	-87	-67	-72	-36			-277	-541
	450	2.66	-38.1	-31.8	-24.2	-20.0	8.3			-29.1	-198	-59	-52					-288	-523
	470	3.07	-36.8	-29.3	-8.3	2.4				-28.0	-168	-51	-41					-297	-505
	480	3.27	-35.6	-26.8	5.8					-28.9	-148	-55	-33					-314	-519

Type	T (°C)	Easy %R _o	Position-specific ¹³ C isotope of C ₃ H ₈ (‰)					
			$\delta^{13}\text{C}_{\text{ter}}$	std	$\delta^{13}\text{C}_{\text{cen}}$	std	$\Delta\text{C}_{\text{c-t}}$	std
Hy	310	0.76	-35.9	0.7	-32.3	1.4	3.5	1.5
	340	0.98	-35.8	0.7	-31.3	1.4	4.6	1.5
	360	1.2	-36.1	0.7	-30.1	1.4	6.0	1.6
	370	1.67	-34.2	0.7	-28.8	1.3	5.4	1.5
	370	1.95	-33.9	0.7	-27.6	1.3	6.3	1.5
Anhy	310	0.76	-36.5	0.7	-33.3	1.3	3.3	1.5
	340	0.98	-35.1	0.7	-30.3	1.3	4.8	1.5
	360	1.2	-35.4	0.7	-28.9	1.3	6.5	1.5
	400	1.75	-33.2	0.7	-26.9	1.4	6.3	1.6
	415	2.00	-32.2	0.7	-24.1	1.4	8.1	1.5
	430	2.28	-31.2	0.7	-22.7	1.3	8.5	1.5
	450	2.66	-27.7	0.7	-16.0	1.3	11.7	1.5
	470	3.07	-15.9	0.7	6.3	1.4	22.2	1.6
	480	3.27	-4.7	0.7	25.8	1.3	30.6	1.5